Master's Thesis

Implementation and Verification of Three-Dimensional MOC Transient Solver in Whole-core Transport code STREAM

Khang Hoang Nhat Nguyen

Department of Nuclear Engineering

Graduate School of UNIST

2019

Implementation and Verification of Three-Dimensional MOC Transient Solver in Whole-core Transport code STREAM

Khang Hoang Nhat Nguyen

Department of Nuclear Engineering

Graduate School of UNIST

Implementation and Verification of Three-Dimensional MOC Transient Solver in Whole-core Transport code STREAM

A thesis/dissertation
submitted to the Graduate School of UNIST
in partial fulfillment of the
requirements for the degree of
Master of Science

Khang Hoang Nhat Nguyen

7. 16. 2019

Approved by

Advisor
Deokjung Lee

Implementation and Verification of Three-Dimensional MOC Transient Solver in Whole-core Transport code STREAM

Khang Nguyen Hoang Nhat

This certifies that the thesis/dissertation of Khang Hoang Nhat Nguyen is approved.

7/16/2019

Advisor: Professor Deokjung Lee

Professor Eisung Yoon

Professor Douglas A. Fynan

Abstract

In the state of the art of computer technology, the transient analysis in the nuclear reactor has become on demand of the nuclear engineering field. This thesis presents the development and the preliminary validation of the transient transport capability in STREAM code. The Theta method with the well-known Crank-Nicholsen scheme providing a second-order accurate is then applied to tackle the time integration in the right-hand side of the time-dependent neutron transport. Eventually, the Methods Of Characteristic (MOC) solver in the steady state with excellent performance and accuracy in STREAM is modified with the delayed neutron term to solve the transient cases. Additionally, a multi-group Coarse Mesh Finite Difference (CMFD) accelerator is introduced to alleviate the computational burden of the simulation. The transient problems, namely TD0, TD1, TD2, TD3, TD4 and TD5 in the C5G7-TD benchmark suite are used for verification. The STREAM time-dependent MOC calculation results show good agreement with results of a deterministic transport analysis code, nTRACER with the maximum disparity of the total power level change is 1.22 % for the TD3-4 case. In the 3D cases, with a proposed decusping method, the maximum amplitude of the relative error is about 3.5% between the two deterministic codes. The disparities induced by decusping methods and whole-core transport method are obviously observed and thus are the primary source causing the discrepancies. With this high fidelity to replicate the solution in the time-dependent transport equation, the transient analysis capability of STREAM code has been proved. This work plays as a foundation for the later 3D whole core transient solver accompanied by TH1D feedbacks for practical transient problems.

This page is intentionally left blank

Tables of Contents

List of Figures

List of Tables

I. Introduction

From the nuclear engineering perspective in the design and licensing of the light water reactors, there are raising efforts have been introduced to the development of the numerical methods in transient simulation of a nuclear reactor, which involves solving the time-dependent (TD) Boltzmann equation including the delayed neutrons contribution. Over the last several decades, reactor transients have been modeled and simulated based on the diffusion approximation to the transport equation. Despite the enhance in the computational burden, the diffusion might not fulfill the growing interest in reactor designs and fuels in terms of accuracy and fidelity. Inevitably, the direct neutron transport methods have become superior for nuclear reactor kinetics calculation as a result of steady development in computational technologies.

The in-house UNIST neutron transport code STREAM [1, 2] has been developed since 2013. It is developed on the pursuit to resolve issues in numerical reactor physics and to produce a high-fidelity LWR core calculation and designing program. Previously, STREAM is used in reactor core analysis as the first approach in the conventional two-step approach with downstream nodal diffusion code RAST-K [3]. Until recently, steady- state direct whole core calculation based on 3D MOC/DD [4] has been adopted to STREAM. In this research, the development and the preliminary validation of the transient transport capability problem in STREAM code are presented. The Theta method with the well-known Crank-Nicholsen scheme providing a second-order accurate is then applied to tackle the time integration in the right-hand side of the TD neutron transport. Eventually, the Methods Of Characteristic (MOC) solver in the steady state with excellent performance and accuracy in STREAM is modified with the delayed neutron term to solve the transient cases. As a result, the TD transport problem requires the calculation of a series of fixed source problems at discrete points in time coupled to previous time points through the update of state variables. Additionally, a multi-group CMFD accelerator is introduced to alleviate the computational burden of the simulation.

1.1 Thesis Outline

The remainder of this section is an outline of the following sections. This outline provides a brief summary of the content for each section.

II. Overview of the Neutron Transport and the derivation of the Steady-State MOC

In section 2, the overview and the derivation of the deterministic neutron transport MOC method that is applied to the reactor steady state problems in STREAM are presented. The derivation of the CMFD accelerator coupled with the MOC transport solver, is also introduced.

III. Derivation of the transient MOC

In Section 3, a derivation of the TD MOC is presented with the approximation that the angular flux time derivative is isotropic, which is an efficient approximation and commonly used in the state-

of-the-art nuclear lattice codes. The time integration based on the Theta method and the treatment and solution of the delayed precursor equations are also presented. The derivation includes the analytical solution for the precursor equations based on the time integration technique are presented in this section.

IV. C5G7 TD neutron transport benchmark and code-to-code verification

The overview of the C5G7 TD neutron transport benchmark is presented in Section 4. Accordingly, the numerical results in the total power level changes have been generated by STREAM. Moreover, a decusping method is proposed to overcome the control rod insertion/withdrawal issue in 3D simulation. The verification is a code-to-code approach. In this research, to maintain the consistency, the source for verification is the whole-core neutron transport code nTRACER.

V. Summary, Conclusion and Future work

In the last Section, a summary of the research proposed in this thesis and the conclusions identified in the preceding sections are provided.

II. Overview of Neutron Transport and Derivation of the Steady State MOC

This section will be started with a brief overview of the neutron transport equation, i.e., the Boltzmann equation, to understand the behavior of the neutrons in the nuclear reactors. The derivation of the MOC for the steady state in STREAM is presented after the discussion. Additionally, the derivation of the CMFD accelerator coupled with the MOC solver is also introduced in this section.

2.1 The Boltzmann Transport Equation

The ultimate goal in the neutron transport codes is to solve the Boltzmann transport equation which can be given as in Eq. (2.1):

$$\boldsymbol{\Omega}\nabla\psi(\boldsymbol{r},\boldsymbol{\Omega},E)+\Sigma_t(\boldsymbol{r},E)\psi(\boldsymbol{r},\boldsymbol{\Omega},E)=\int_0^\infty dE'\int_{4\pi}d\boldsymbol{\Omega}'\Sigma_s(\boldsymbol{r},\boldsymbol{\Omega}'\rightarrow\boldsymbol{\Omega},E'\rightarrow E)\psi(\boldsymbol{r},\boldsymbol{\Omega}',E') + \frac{\chi(\boldsymbol{r},E)}{4\pi k_{eff}}\int_0^\infty dE'\nu\Sigma_f(\boldsymbol{r},E')\int_{4\pi}d\boldsymbol{\Omega}'\psi(\boldsymbol{r},\boldsymbol{\Omega}',E')\,. \tag{2.1}$$

where:

- $\boldsymbol{r}$: Spatial position vector,
- $\boldsymbol{\Omega}$: Angular direction vector,
- E: Neutron energy,
- ψ: Angular neutron flux,
- k_{eff}: Effective neutron multiplication factor,
- Σ_t: Neutron total cross-section,
- Σ_a: Neutron absorption cross-section,
- Σ_f: Neutron fission cross-section,
- χ: Fission neutron energy spectrum,
- ν: Average number of neutrons emitted per fission event.

To simplify the equation, the right-hand side (RHS) terms are collected as the total neutron source $Q(\boldsymbol{r},\boldsymbol{\Omega},E)$:

$$Q(\boldsymbol{r},\boldsymbol{\Omega},E)=\int_0^\infty dE'\int_{4\pi}d\boldsymbol{\Omega}'\Sigma_s(\boldsymbol{r},\boldsymbol{\Omega}'\rightarrow\boldsymbol{\Omega},E'\rightarrow E)\psi(\boldsymbol{r},\boldsymbol{\Omega}',E') + \frac{\chi(\boldsymbol{r},E)}{4\pi k_{eff}}\int_0^\infty dE'\nu\Sigma_f(\boldsymbol{r},E')\int_{4\pi}d\boldsymbol{\Omega}'\psi(\boldsymbol{r},\boldsymbol{\Omega}',E')\,. \tag{2.2}$$

Then the transport equation can be abbreviated as:

$$\boldsymbol{\Omega}\nabla\psi(\boldsymbol{r},\boldsymbol{\Omega},E)+\Sigma_t(\boldsymbol{r},E)\psi(\boldsymbol{r},\boldsymbol{\Omega},E)=Q(\boldsymbol{r},\boldsymbol{\Omega},E)\,. \tag{2.3}$$

Although the solution of the equation 2.1 is the angular flux, we are often interested in the neutron scalar flux $\phi(\boldsymbol{r},E)$, which is calculated as the integration of the angular flux over all angles:

$$\phi(\boldsymbol{r}, E) = \int_{4\pi} \psi(\boldsymbol{r}, \boldsymbol{\Omega}, E)\, d\boldsymbol{\Omega}\,. \tag{2.4}$$

Predicting the neutron flux distribution in a reactor is the major concerns of nuclear reactor physics because the neutron flux is essential for the nuclear reaction rates calculation. These reaction rates can illustrate essential characteristics of the nuclear reactor such as the fission source amplitude, the number of actinides is generated, the impact of the radiation on the materials of the reactor vessels. Techniques to solve the neutron transport equation are typically classified by the treatment of the angular and spatial variables. In the following section is the derivation of the MOC technique for solving the neutron transport equation.

2.2 Derivation of the MOC for steady state

The MOC method treats the angular dependence of the neutron flux by introducing the discrete ordinates along the path which neutrons travel. Similar to the Collision Probability Method (CPM) [5], MOC can be applied for complex geometries with rays, which is coined as characteristics, along where the neutron flux is propagated.

The characteristic form of the Eq. (2.3) can be found based on the use of the characteristic curves, namely:

$$\boldsymbol{r} = \boldsymbol{r_0} + s\boldsymbol{\Omega}\,. \tag{2.5}$$

For any location $\boldsymbol{r}$ of interest, each angular direction vector $\boldsymbol{\Omega}$' is matched to a corresponding reference location $\boldsymbol{r_0'}$ defined using Eq. (2.5) as $\boldsymbol{r} = \boldsymbol{r_0'} + s\boldsymbol{\Omega}'$. This parametrization for the position can be inserted to the transport equation in Eq. (2.2) and Eq. (2.3) as:

$$\begin{aligned} Q(\boldsymbol{r_0} + s\boldsymbol{\Omega}, \boldsymbol{\Omega}, E) = &\int_0^\infty dE' \int_{4\pi} d\boldsymbol{\Omega}' \Sigma_s(\boldsymbol{r_0'} + s\boldsymbol{\Omega}', \boldsymbol{\Omega}' \to \boldsymbol{\Omega}, E' \to E)\psi(\boldsymbol{r_0'} + s\boldsymbol{\Omega}', \boldsymbol{\Omega}', E') \\ &+ \frac{\chi(\boldsymbol{r_0'} + s\boldsymbol{\Omega}', E)}{4\pi k_{eff}} \int_0^\infty dE' \nu\Sigma_f(\boldsymbol{r_0'} + s\boldsymbol{\Omega}', E') \int_{4\pi} d\boldsymbol{\Omega}' \psi(\boldsymbol{r_0'} + s\boldsymbol{\Omega}', \boldsymbol{\Omega}', E')\,, \end{aligned} \tag{2.6}$$

$$\boldsymbol{\Omega}\nabla\psi(\boldsymbol{r_0} + s\boldsymbol{\Omega}, \boldsymbol{\Omega}, E) + \Sigma_t(\boldsymbol{r_0} + s\boldsymbol{\Omega}, E)\psi(\boldsymbol{r_0} + s\boldsymbol{\Omega}, \boldsymbol{\Omega}, E) = Q(\boldsymbol{r_0} + s\boldsymbol{\Omega}, \boldsymbol{\Omega}, E)\,. \tag{2.7}$$

Applying the differential operator to the angular flux in Eq. (2.7) yields:

$$\frac{d}{ds}\psi(\boldsymbol{r_0} + s\boldsymbol{\Omega}, \boldsymbol{\Omega}, E) + \Sigma_t(\boldsymbol{r_0} + s\boldsymbol{\Omega}, E)\psi(\boldsymbol{r_0} + s\boldsymbol{\Omega}, \boldsymbol{\Omega}, E) = Q(\boldsymbol{r_0} + s\boldsymbol{\Omega}, \boldsymbol{\Omega}, E)\,. \tag{2.8}$$

The dependence of s on the position vector and the angular flux $\boldsymbol{r_0} + s\boldsymbol{\Omega}$ will be referred as $\boldsymbol{s}$ such that the characteristic equation can be simply rewritten as:

$$\frac{d}{ds}\psi(\boldsymbol{s}, \boldsymbol{\Omega}, E) + \Sigma_t(\boldsymbol{s}, E)\psi(\boldsymbol{s}, \boldsymbol{\Omega}, E) = Q(\boldsymbol{s}, \boldsymbol{\Omega}, E)\,. \tag{2.9}$$

This first order differential equation can be solved by the method of Lagrange with the analytical solution given in Eq. (2.10):

$$\psi(\boldsymbol{s},\boldsymbol{\Omega},E)=\psi(\boldsymbol{s_0},\boldsymbol{\Omega},E)e^{-\int_0^s ds'\Sigma_t(s',E)}+\int_0^s d\boldsymbol{s}''Q(\boldsymbol{s}'',\boldsymbol{\Omega},E)e^{-\int_{s''}^s ds'\Sigma_t(s',E)}. \tag{2.10}$$

In Eq. (2.10), all the parameters are defined as functions of continuous neutron energy, which leads to the difficulty in achieving the solution directly. To overcome this obstacle, the multi-group approximation is introduced by discretizing the energy domain into distinct energy groups. By applying the same procedure mentioned above, the solution to the multi-group characteristic neutron transport equation for an energy group g is given:

$$\psi^g(\boldsymbol{s},\boldsymbol{\Omega})=\psi^g(\boldsymbol{s_0},\boldsymbol{\Omega})e^{-\int_0^s ds'\Sigma_t^g(s')}+\int_0^s d\boldsymbol{s}''Q^g(\boldsymbol{s}'',\boldsymbol{\Omega})e^{-\int_{s''}^s ds'\Sigma_t^g(s')}, \tag{2.11}$$

where the neutron source is given as:

$$\begin{aligned}Q^g(\boldsymbol{s},\boldsymbol{\Omega})=&\sum_{g'=1}^{G}\int_{4\pi}d\boldsymbol{\Omega}'\Sigma_s^{g'\to g}(\boldsymbol{s},\boldsymbol{\Omega}'\to\boldsymbol{\Omega})\psi^{g'}(\boldsymbol{s},\boldsymbol{\Omega}')\\&+\frac{\chi^g(\boldsymbol{s})}{4\pi k_{eff}}\sum_{g'=1}^{G}\nu\Sigma_f^{g'}(\boldsymbol{s})\int_{4\pi}d\boldsymbol{\Omega}'\psi^{g'}(\boldsymbol{s},\boldsymbol{\Omega}').\end{aligned} \tag{2.12}$$

where the condensed cross-sections are achieved from the pin-wised slowing down method [1].

The discrete ordinates approximation is then introduced to approximate the integral over the angular domain in the neutron source and in the angular flux. Further decomposition into polar and azimuthal angles is also made for the angular flux and the neutron source for each quadrature points. Another standard approximation for MOC is to assume that the source Q^g is constant across discrete spatial cells, termed *flat source regions* (FSRs) illustrated in Fig. 1. Utilizing above approximations and discretization methods, for a projected streaming track on the x-y plane shown in Fig. 2, the solution in Eq. (10) for the azimuthal angle i, polar angle j in the FSR m with the segment (track) k can be given as:

$$\psi_{i,j,k}^g(s)=\psi_{i,j,k}^g(0)e^{-\frac{\Sigma_{tr,m}^g}{\cos(\theta_j)}s}+\frac{Q_{i,j,m}^g}{\Sigma_{tr,m}^g}\left(1-e^{-\frac{\Sigma_{tr,m}^g}{\cos(\theta_j)}s}\right). \tag{2.13}$$

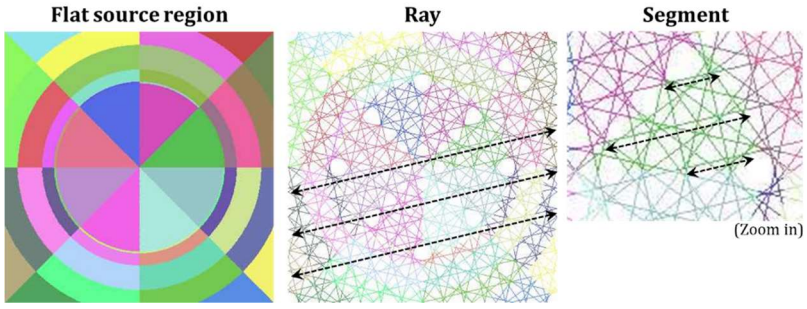

Figure 1 Discretization Scheme for a pin-cell problem

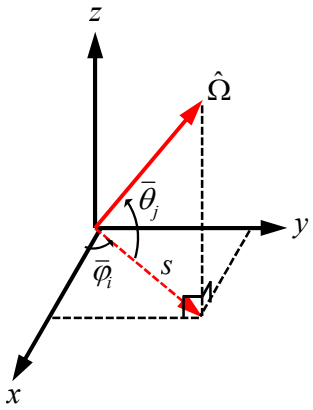

Figure 2 A streaming track projected on the x-y plane

One can note that the neutron total cross-section is replaced with the transport corrected cross-section because the contribution of the anti-isotropic source is assumed to be insignificant; therefore, the scattering source is isotropic. The neutron source in Eq. (2.12) is then given as:

$$Q_{i,j,m}^{g} = \frac{1}{4\pi}\left(\frac{\chi_m^g}{k_{eff}}\sum_{g'=1}^{G}\nu\Sigma_{f,m}^{g'}\phi_m^{g'} + \sum_{g'=1}^{G}\Sigma_{m,s}^{g'\to g}\phi_m^{g'}\right). \tag{2.14}$$

where the integrated angular flux ϕ_m^g is termed the scalar flux for the FSR m.

Let take a segment with a length of $t'_{i,j,k}$ into consideration which is illustrated in Fig.3, the outgoing angular flux can be expressed as:

$$\psi_{i,j,k}^{g,out} = \psi_{i,j,k}^{g,in}e^{-\Sigma_{tr,m}^{g}t'_{i,j,k}} + \frac{Q_{i,j,m}^{g}}{\Sigma_{tr,m}^{g}}\left(1 - e^{-\Sigma_{tr,m}^{g}t'_{i,j,k}}\right). \tag{2.15}$$

where $t_{i,j,k}$ is the length of the track projected on x-y plane and $t'_{i,j,k} = \frac{t_{i,j,k}}{\cos(\theta_j)}$

Figure 3 Outgoing angular flux for a segment length t'

To identify the parameter remaining, the integral over the area for the FSR area-averaged scalar flux, the segments area approximation is introduced. Firstly, the segment-average angular flux is expressed in Eq. (2.16):

$$\bar{\psi}_{i,j,k}^{g} = \frac{\int_0^{t'_{i,j,k}}\psi_{i,j,k}^{g}(s)ds}{\int_0^{t'_{i,j,k}}ds} = \frac{\int_0^{t'_{i,j,k}}\psi_{i,j,k}^{g}(0)e^{-\Sigma_{tr,m}^{g}s} + \frac{Q_{i,j,m}^{g}}{\Sigma_{tr,m}^{g}}\left(1 - e^{-\Sigma_{tr,m}^{g}s}\right)ds}{t'_{i,j,k}} \tag{2.16}$$

$$= \frac{Q_{i,j,m}^{g}}{\Sigma_{tr,m}^{g}} + \frac{\Delta_{i,j,k}^{g}}{\Sigma_{tr,m}^{g}t'_{i,j,k}},$$

with $\Delta_{i,j,k}^{g} = \psi_{i,j,k}^{g}(0) - \psi_{i,j,k}^{g}(t'_{i,j,k}) = \psi_{i,j,k,in}^{g} - \psi_{i,j,k,out}^{g}$ is the change in the angular flux along

the segment. Then the integration for all of available segments in a FSR m yields the region-averaged angular flux as:

$$\bar{\bar{\psi}}_{i,j,m}^{g} = \frac{\sum_{k\in m} \bar{\psi}_{i,j,k}^{g} t'_{i,j,k} d_i}{\sum_{k\in m} t'_{i,j,k}\, d_i}, \tag{2.17}$$

where d_i denotes for the ray distance of the MOC calculation.

With the isotropic assumption in the flux, the neutron scalar flux can be given as in Eq. (2.18). The contributions of the azimuthal and polar angles to the scalar flux are denoted by ω_i and ω_j respectively.

$$\begin{aligned} \phi_m^g &= 4\pi \sum_j \sum_i \bar{\bar{\psi}}_{i,j,m}^{g}\, \omega_i \omega_j \\ &= \frac{4\pi}{\Sigma_{tr,m}^{g}} \left(Q_{i,j,m}^{g} + \frac{1}{A_m} \sum_j \sum_i \sum_{k\in m} \Delta_{i,j,k}^{g} d_i \omega_i \omega_j \cos\left(\bar{\theta}_j\right) \right). \end{aligned} \tag{2.18}$$

Although MOC proves itself with many advantages including treatment of complex geometries and amenability for parallelization, the slow convergence behavior is it drawback which necessitates the significant incentive to have an accelerator to alleviate the computational time is inevitable. Various acceleration schemes have been proposed for MOC with (Coarse Mesh Finite Difference) CMFD being the most widely adopted due to its simplicity and acceleration performance. In the following section, the formulation of the CMFD is introduced.

2.3 The CMFD as an acceleration

CMFD was first proposed by Smith [6] and has been widely used in accelerating neutron diffusion and transport problems. Particularly, it has been shown that CMFD acceleration gives the speedup factor to 100 times than using MOC standalone solver [7].

By using the CMFD formulation, it is possible to construct a pin-cell based (coarse mesh) diffusion problem equivalent to the flat-source regions (fined mesh) transport problem. The obtained solution from the diffusion problem can accelerate the convergence of the transport problem. Fig. 4 is an example of the FSRs mesh layout, and the coarse mesh layout used for a 16 by 16 fuel assembly (FA) problem.

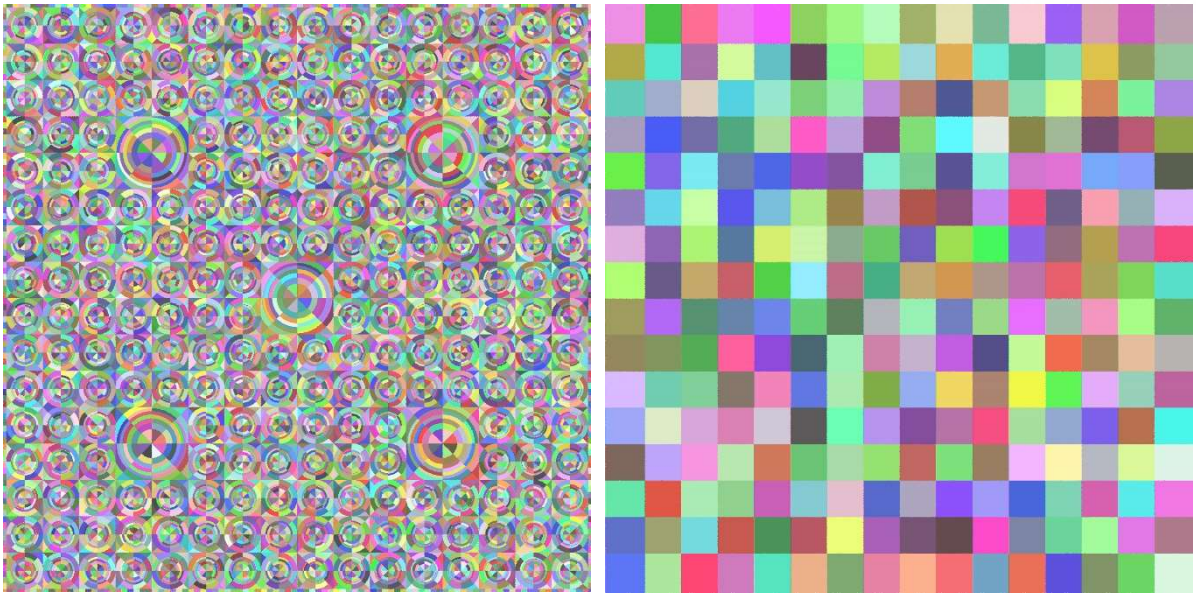

Figure 4 FSR (left) and CMFD (right) layout for a 16 x 16 FA

For the derivation of the CMFD, the steady-state multi-group neutron diffusion equation is expressed in Eq. (2.19):

$$-\nabla \cdot D^g(x,y,z)\phi^g(x,y,z) + \Sigma_a^g(x,y,z)\phi^g(x,y,z) + \sum_{\substack{g'=1 \\ g' \neq g}}^{G} \Sigma_s^{g \to g'}(x,y,z)\phi^g(x,y,z)$$
$$= \frac{\chi^g(x,y,z)}{k_{eff}} \sum_{g'=1}^{G} \nu\Sigma_f^{g'}(x,y,z)\phi^{g'}(x,y,z) + \sum_{\substack{g'=1 \\ g' \neq g}}^{G} \Sigma_s^{g' \to g}(x,y,z)\phi^{g'}(x,y,z)\,. \tag{2.19}$$

where

- D: Diffusion coefficient,
- Σ_a^g: Coarse mesh absorption cross-section for energy group g,
- Σ_f^g: Coarse mesh fission cross-section for energy group g,
- $\Sigma_s^{g \to g'}$: Coarse mesh down-scattering cross-section for energy group g,
- $\Sigma_s^{g' \to g}$: Coarse mesh up-scattering cross-section for energy group g,
- ϕ: Scalar flux in the coarse mesh node,
- χ: Fission spectrum,
- k_{eff}: Neutron multiplication factor,
- ν: Average number of neutrons emitted per fission event,
- x, y, z: Positional variables. For the sake of simplicity, these variables are now referred to a computational node m.

In the formulation of the CMFD diffusion problem, cell homogenized constants and currents correction coefficients are required. Below section presents the homogenization and coefficient

calculation process.

a) Cross section condensation

The cross sections for the CMFD diffusion equation are generated by energy-condensation and area-averaging of the cross sections from the fine mesh as shown in below equations:

$$\Sigma_{a,m}^{\bar{g}} = \frac{\sum_{g\in\bar{g}}\sum_{r\in m}\Sigma_{a,r}^{g}\phi_r^g A_r}{\sum_{g\in\bar{g}}\sum_{r\in m}\phi_r^g A_r}, \tag{2.20}$$

$$\Sigma_{tr,m}^{\bar{g}} = \frac{\sum_{g\in\bar{g}}\sum_{r\in m}\Sigma_{tr,r}^{g}\phi_r^g A_r}{\sum_{g\in\bar{g}}\sum_{r\in m}\phi_r^g A_r}, \tag{2.21}$$

$$\Sigma_{s,m}^{\bar{g}\to\bar{g}'} = \frac{\sum_{g\in\bar{g}}\sum_{g'\in\bar{g}'}\sum_{r\in m}\Sigma_{s,r}^{g\to g'}\phi_r^g A_r}{\sum_{g\in\bar{g}}\sum_{r\in m}\phi_r^g A_r}, \tag{2.22}$$

$$\nu\Sigma_{f,m}^{\bar{g}} = \frac{\sum_{g\in\bar{g}}\sum_{r\in m}\nu\Sigma_{f,r}^{g}\phi_r^g A_r}{\sum_{g\in\bar{g}}\sum_{r\in m}\phi_r^g A_r}, \tag{2.23}$$

$$\chi_m^{\bar{g}} = \frac{\sum_{g\in\bar{g}}\sum_{r\in m}\chi_r^g\sum_{g_1=1}^{G}\nu\Sigma_{f,r}^{g1}\phi_r^{g1}A_r}{\sum_{\bar{g}2=1}^{\bar{G}}\sum_{g\in\bar{g}2}\sum_{r\in m}\chi_r^g\sum_{g_1=1}^{G}\nu\Sigma_{f,r}^{g1}\phi_r^{g1}A_r}, \tag{2.24}$$

$$D_m^{\bar{g}} = \frac{\sum_{g\in\bar{g}}\frac{1}{3\Sigma_{tr,m}^{g}}\phi_{g,CMFD}^{i,j}}{\sum_{g\in\bar{g}}\phi_{g,CMFD}^{m}}, \tag{2.25}$$

$$\phi_{g,CMFD}^{m} = \frac{\sum_{r\in m}\phi_r^g A_r}{\sum_{r\in(i,j)}A_r}, \tag{2.26}$$

and

$$\phi_{\bar{g}}^{m} = \sum_{g\in\bar{g}}\phi_{g,CMFD}^{m}\,. \tag{2.27}$$

where

- $\bar{g}$: Index of CMFD neutron energy group structure with $\bar{G}$ groups in total,
- A: Denotation for the area of the cell of interest.

b) Solving the diffusion problem

The Finite Difference Method (FDM) is then applied to solve the diffusion problem given in Eq. (2.19). To maintain the consistency, the superscript g in Eq. (2.19) will be changed into $\bar{g}$ from now on. By expansion of the diffusion coefficient D into the spatial direction and minor rearrangement, the spatially discretized diffusion equation Eq. (2.19) can be solved. Here we use a 1D expression for simplicity:

$$\frac{\left(J_{m+}^{\bar{g}} - J_{m-}^{\bar{g}}\right)}{\Delta m} + \Sigma_{r,m}^{\bar{g}}\phi_m^{\bar{g}} = \frac{\chi_m^{\bar{g}}}{k_{eff}} \sum_{\bar{g}'=1}^{\bar{G}} \nu\Sigma_{f,m}^{\bar{g}'}\phi_m^{\bar{g}'} + \sum_{\substack{\bar{g}'=1 \\ \bar{g}' \neq g}}^{\bar{G}} \Sigma_{s,m}^{\bar{g}' \to \bar{g}}\phi_m^{\bar{g}'}\,, \tag{2.28}$$

with the removal cross-section is defined as:

$$\Sigma_{r,m}^{\bar{g}} = \Sigma_{a,m}^{\bar{g}} + \sum_{\substack{\bar{g}'=1 \\ \bar{g}' \neq \bar{g}}}^{\bar{G}} \Sigma_{s,m}^{\bar{g} \to \bar{g}'}\,. \tag{2.29}$$

and Δm is the width of the cell, $J_{m\pm}^{\bar{g}}$ is the neutron current at each cell surface.

Please note that in the Eq. (2.29), the net current is the algebraic expression based on the finite difference approximation being applied across the surface of the two adjacent cells and not the actual net current in the MOC problem. The actual current from the MOC problem is computed by accumulating the current contribution from every segment that crosses a surface. To preserve the neutron current in the surface of the CMFD problem, a new correction factor $\widehat{D}$ is added as:

$$J_{m\pm}^{\bar{g}} = -\widehat{D}_{m\pm}^{\bar{g}}\left(\phi_{m\pm1}^{\bar{g}} + \phi_{i,j}^{\bar{g}}\right) \mp \widetilde{D}_{i+\frac{1}{2},j}^{\bar{g}}\left(\phi_{m\pm1}^{\bar{g}} - \phi_{i,j}^{\bar{g}}\right), \tag{2.30}$$

where the current from the MOC given as:

$$J_{m\pm}^{\bar{g}} = \frac{4\pi}{\Delta m}\sum_{p}\sum_{az}\sum_{k\in m}\sum_{g\in\bar{g}} \psi_{az,p,k,m\pm}^{g} d_{az}\omega_{az}\omega_p \cos\left(\overline{\theta_p}\right). \tag{2.31}$$

Upon convergence of the CMFD diffusion problem, prolongation is then performed by multiplying each FSR's scalar flux by the ratio of the converged coarse mesh scalar flux to the initial coarse mesh scalar flux in the acceleration step:

$$\phi_{MOC\ node}^{g} = \phi_{MOC\ node}^{g} \times \frac{\phi_{\bar{g},updated\ after\ CMFD}^{m}}{\phi_{\bar{g},initial\ before\ CMFD}^{m}}\ (MOC\ node \in m\ node\ in\ CMFD)\,. \tag{2.32}$$

The convergence is evaluated based on several measures, including the convergence of the eigenvalue, the residual, the fission source. The calculation flow can be summarized in Fig. 5.

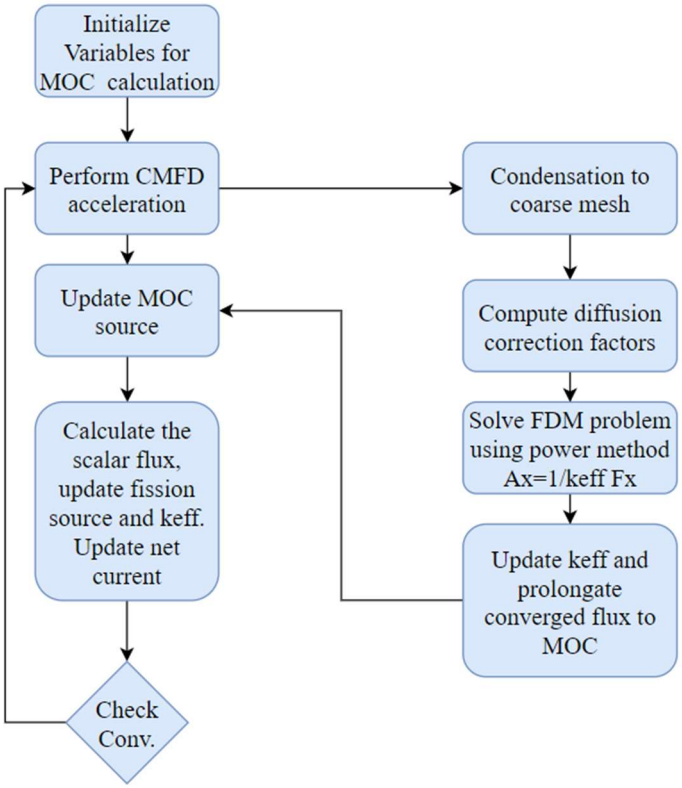

Figure 5 The iteration scheme to solve the transport problem using MOC with CMFD as an acceleration

III. Derivation for MOC transient state calculation

The typical approach to solve the time-dependent neutron transport equation is to discretize the equation in time and apply a time integration technique to treat the time derivative. Although there are many time integration methods available, they generally result in one or more equations of similar form to the steady-state transport equation but with a transient fixed source term resulting from a finite difference approximation of the time derivative and the delayed neutron source. The TD MOC based form of the transport problem is given as:

$$\frac{1}{v_m^g}\frac{d\psi_{i,j,k}^g(s,t)}{dt} = -\cos(\bar{\theta}_j)\frac{d\psi_{i,j,k}^g(s,t)}{ds} - \Sigma_{tr,m}^g\psi_{i,j,k}^g(s,t) + Q_{i,j,m}^g(t)\,, \tag{3.1}$$

where the isotropic neutron source is given as:

$$Q_{i,j,m}^g(t) = \frac{1}{4\pi}\left[\chi_{p,m}^g \times (1-\beta) \times S_{F,m}(t) + \sum_{g'}\Sigma_{s,m}^{g'\to g}\phi_m^{g'}(t) + \chi_{d,m}^g S_{d,m}(t)\right], \tag{3.2}$$

where

- $\chi_{d,m}^g$ is the delayed neutron spectrum,
- $S_{F,m}(t) = \frac{1}{k_{eff}}\sum_{g'}\nu\Sigma_{f,m}^{g'}\phi_m^{g'}(t)$,

- β is the total delayed neutron fraction,
- v_m^g is the neutron velocity.

The delayed neutron source for a flat source region $S_{d,m}$ is the accumulated contribution of the delayed neutron precursors:

$$S_{d,m}(t) = \sum_l \lambda_l C_{l,m}(t)\,, \tag{3.3}$$

where l is the delayed neutron precursors group index, and typically in nuclear reactor transient analysis, the number of delayed neutron precursor is six, and the delayed neutron precursors density for group l, $C_{l,m}(t)$, can be described by Eq. (3.4);

$$\frac{dC_{l,m}(t)}{dt} = \beta_l S_{F,m}(t) - \lambda_l C_{l,m}(t)\,, \tag{3.4}$$

where

- λ_l is the delay constant for delayed neutron precursor group l,
- $C_{l,m}$ is the delayed neutron precursor concentration of group l,
- β_l is the group l delayed neutron precursor yield and be assumed to be independent of time.

Because storing the angular flux from one or more previous time steps to represent the angular flux time derivative for using in the time integration technique is massively memory-intensive for a typical nuclear reactor problem. Several pieces of research have been conducted and investigated for a proper approximation of the angular dependence of the angular flux time derivative to reduce the computational memory of the time-dependent neutron transport problem. In our research, the isotropic angular flux time derivative [8, 9, 10], which is a low-order angular approximation is used. The angular flux derivative can be expressed by the scalar flux as followed:

$$\frac{1}{v_m^g}\frac{d\psi_{i,j,k}^g(s,t)}{dt} = \frac{1}{4\pi v_m^g \Delta}\frac{\phi_m^g(t)}{dt}\,. \tag{3.5}$$

By storing the scalar flux instead of the angular flux, the computational memory requirement is productively reduced. This approximation is very efficient and attractive to the transient transport calculation [8, 9].

In order to reuse the steady-state solver, a modification is necessary to introduce for the RHS of the Eq. (3.1) which is shown in the below section, including the time integration based on the Theta method and the delayed neutron precursor equation solution.

3.1 Temporal discretization

At a given time-step size Δt_n for a time step t_n, Eq. (3.1) can be discretized using the Theta method as follow:

$$\frac{1}{4\pi v_m^g \Delta t_n}\left(\phi_m^{n,g} - \phi_m^{n-1,g}\right) = \theta R_m^{n,g} + (1-\theta) R_m^{n-1,g}\,, \tag{3.6}$$

where the expression $R_m^{n,g}$ denoting RHS terms in Eq. (3.1) at the time step t_n. With $\theta > 0$, by diving θ in both side of Eq. (3.6), it can be rewritten as:

$$\frac{1}{4\pi v_m^g \Delta t_n \theta}\left(\phi_m^{n,g} - \phi_m^{n-1,g}\right) = R_m^{n,g} + \left(\frac{1}{\theta} - 1\right) R_m^{n-1,g}\,. \tag{3.7}$$

For the Crank-Nicholsen scheme [9], $\theta = 0.5$. The superscript $n-1$ indicates the known variables from the previous time step, so only the flux at the current time step is unknown and need to be achieved.

3.2 Delayed neutron precursor time integration

Since the $R_m^{n,g}$ term contains the delayed neutron source term which involves the unknown delayed neutron precursor concentrations at time step t_n, which is required time differencing to solve, it is impossible to solve Eq. (34) directly. To overcome this obstacle, the approximation to solve the delayed neutron precursor equation [11, 12] is performed as followed.

Firstly, let multiply $C_{l,m}(t)$ with $e^{\lambda_l t}$ then take the derivative and insert Eq. (3.4) yields:

$$\frac{d\left(C_{l,m}(t) \times e^{\lambda_l t}\right)}{dt} = e^{\lambda_l t}\frac{dC_{l,m}(t)}{dt} + \lambda_l e^{\lambda_l t} C_{l,m}(t) = e^{\lambda_l t}\beta_l S_{F,m}(t)\,. \tag{3.8}$$

By using the second-order approximation for $S_{F,m}(t)$:

$$\begin{aligned}\beta_l S_{F,m}(t) \approx{}& \beta_l^n S_{F,m}^n \frac{\tilde{t}^2 + \tilde{t}\gamma\Delta t_n}{(1+\gamma)(\Delta t_n)^2} + \beta_l^{n-1} S_{F,m}^{n-1}\left(1 - \frac{(\tilde{t}^2 + (\gamma-1)\Delta t_n \tilde{t})}{\gamma(\Delta t_n)^2}\right)\\ &+\beta_l^{n-2} S_{F,m}^{n-2}\frac{\tilde{t}^2 - \tilde{t}\Delta t_n}{(1+\gamma)\gamma(\Delta t_n)^2}; \tilde{t} = t - t_{n-1}; \gamma = \frac{\Delta t_{n-1}}{\Delta t_n}\quad .\end{aligned} \tag{3.9}$$

with n is the index of time-step.

Take the integration of the Eq. (3.9) over time step t_n, the solution for the delayed neutron precursor concentration $C_{l,m}^n$ can be expressed through $S_{F,m}^n$ as:

$$C_{l,m}^n = \Omega_l^0\left(\tilde{\lambda}_l^n\right) C_{l,m}^{n-1} + \frac{1}{\lambda_l^n}\sum_{t=0}^{2} \beta_l^{n-t} S_{F,m}^{n-t} \Omega_l^{n-t}\left(\tilde{\lambda}_l^n\right), \tag{3.10}$$

where

$$\begin{aligned}&\Omega_l^0\left(\tilde{\lambda}_l^n\right) = e^{-\lambda_l^n \Delta t_n}; \tilde{\lambda}_l^n = \lambda_l^n \Delta t_n; \kappa_0(x) = 1 - e^{-x}\,,\\ &\kappa_1(x) = 1 - \frac{\kappa_0(x)}{x}; \kappa_2(x) = 1 - \frac{2\kappa_1(x)}{x}\,,\end{aligned} \tag{3.11}$$

$$\Omega_l^n\left(\tilde{\lambda}_l^n\right) = \frac{\left(\kappa_2\left(\tilde{\lambda}_l^n\right) + \gamma\kappa_1\left(\tilde{\lambda}_l^n\right)\right)}{1+\gamma}, \tag{3.12}$$

$$\Omega_l^{n-1}\left(\tilde{\lambda}_l^n\right) = \kappa_0\left(\tilde{\lambda}_l^n\right) - \frac{\left(\kappa_2\left(\tilde{\lambda}_l^n\right) + (\gamma-1)\kappa_1\left(\tilde{\lambda}_l^n\right)\right)}{\gamma}, \tag{3.13}$$

and

$$\Omega_l^{n-2}\left(\tilde{\lambda}_l^n\right) = \frac{\left(\kappa_2\left(\tilde{\lambda}_l^n\right) - \kappa_1\left(\tilde{\lambda}_l^n\right)\right)}{(1+\gamma)\gamma}. \tag{3.14}$$

By using the solution in Eq. (3.12), (3.13) and (3.14), the delayed neutron source can be expressed as:

$$S_{d,m}^n = \sum_l \lambda_l C_{l,m}^n = \omega^n S_{F,m}^n + \tilde{S}_{d,m}^{n-1}, \tag{3.15}$$

where

$$\omega^n = \sum_l \beta_l^n \Omega_l^n\left(\tilde{\lambda}_k^n\right), \tag{3.16}$$

$$\tilde{S}_{d,m}^{n-1} = \sum_l \lambda_l \Omega_l^0\left(\tilde{\lambda}_k^n\right) C_{l,m}^{n-1} + \sum_{t=0}^{2} \beta_l^{n-t} S_{F,m}^{n-t} \Omega_l^{n-t}\left(\tilde{\lambda}_l^n\right). \tag{3.17}$$

By inserting the delayed neutron source terms determined by the previous time step values, Eq. (3.17), into Eq. (3.9), the transient fixed source problem can be expressed as follow:

$$\cos\left(\bar{\theta}_j\right)\frac{d\psi_{i,j,k}^{n,g}(s)}{ds} = \Sigma_{t,m}^{\mathrm{g}}\psi_{i,j,k}^{n,g}(s) + Q_{i,j,m}^{n,g}, \tag{3.18}$$

where the modification source for the MOC transport solver at time step t_n, $Q_{i,j,m}^{n,g}$, is given as:

$$Q_{i,j,m}^{n,g} = \left(\frac{1}{\theta} - 1\right) R_m^{n-1,g} - \frac{1}{4\pi v_m^g \Delta t_n \theta}\left(\phi_m^{n,g} - \phi_m^{n-1,g}\right)$$

$$+ \frac{1}{4\pi}\left[\chi_{p,m}^g \times (1-\beta) \times S_{F,m}^n + \sum_{g'} \Sigma_{s,m}^{g'\to g} \phi_m^{n,g'}(t) + \chi_{d,m}^g\left(\omega^n S_{F,m}^n + \tilde{S}_{d,m}^{n-1}\right)\right]. \tag{3.19}$$

By reusing the solver from the steady state with the modified source term, the transient problems can be solved as a series of fixed source problems at each time step. The source term consists of three terms: the previous flux term, the delayed neutron source term, and the residual term. The residual term representing the imbalance at the previous time should be evaluated to establish the fixed source problem. Since the cross sections and other constants must be updated at the beginning of each time step, it is better to calculate the residual at the end of the time step for use in the next time step. As

was the case using MOC algorithm, the CMFD accelerator for the steady-state and the time-dependent problems are similar. The main differences are the separation in the source with the fission source from prompt and delayed neutrons and the presence of the temporal flux derivative. The time-dependent CMFD can be used as the same procedure in the steady-state. The transient calculation process can be express through the flow chart in Fig. 6.

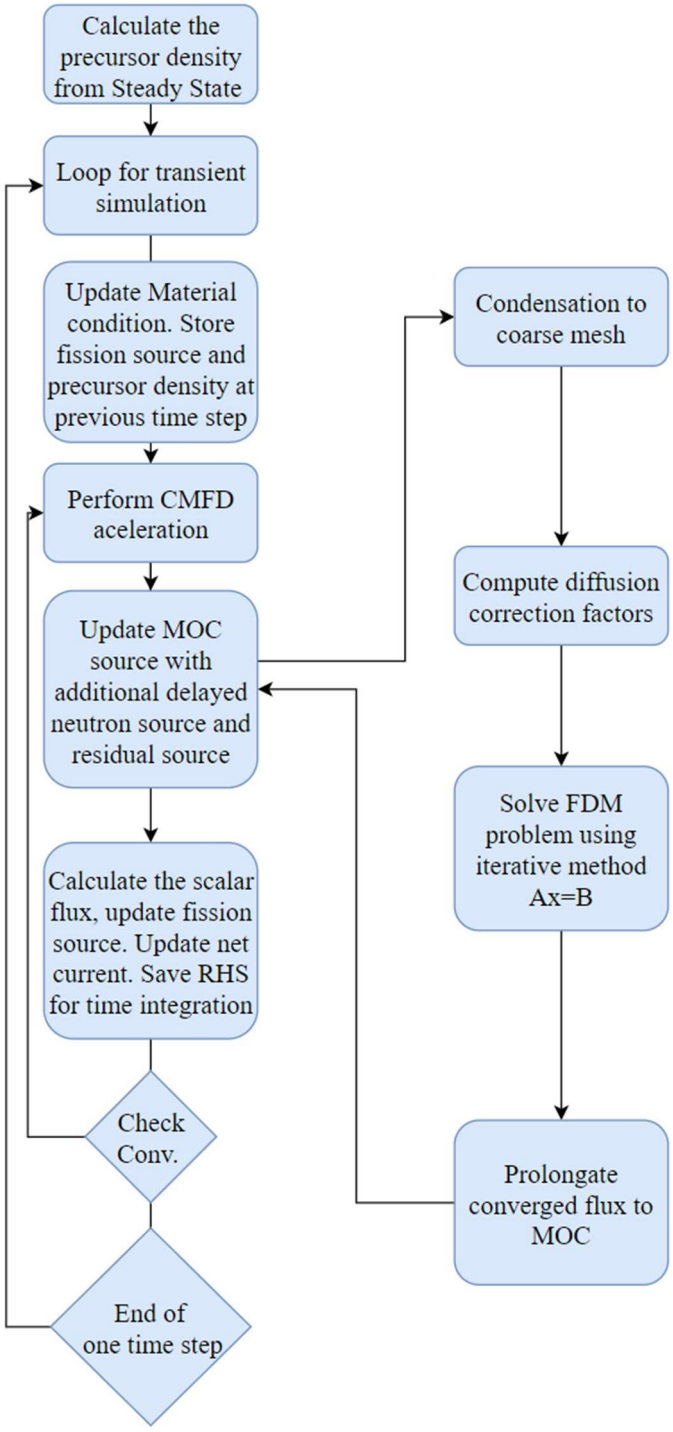

Figure 6 The iteration scheme to solve the transient problem using MOC with CMFD as an acceleration

IV. Verification of the transient capability using the C5G7-TD transient benchmark

4.1 Benchmark description

This section provides a brief overview of the benchmark description and the transient exercises within the benchmark. The time-dependent benchmark is an extension from the C5G7-MOX benchmark [13]. The core in this benchmark is a simplified quarter-core configuration containing two MOX and two UO2 fuel assemblies. This benchmark is selected for this verification because it is a simple model and has a well-known reputation in the verification of the transient capability for a time-dependent transport code. The water is used as reflector both in axial and radial side of the core with the control rod initially located in the top reflector area. The core configuration is illustrated in Fig.7. The fuel assemblies used in this benchmark are based on the Westinghouse 17x17 type, containing 264 fuel pins, 24 guide tubes for control nodes and one instrument tube for a fission chamber in the center of the assembly as illustrated in Fig. 7. The dimension of all pin cells is 0.54 cm in the radius with a pin pitch of 1.26 cm. The cladding material in this benchmark is homogenized with the fuel material. Three enrichment levels are used for the MOX assemblies, namely 4.3 %, 7.0%, and 8.7%. For the UO2 fuel assembly, it is loaded uniformly with 3.7% enriched fuel.

There are 6 transient exercises, namely TD0-TD5, with the brief description given in Table. I. Within each exercise, the control rods banks inserted for each assembly or the moderator density are varied. Except for the TD0 exercise using step insertion and removals of the control rods, the others use linear changing in the reactivity.

Table. I Brief Description of C5G7-TD Benchmark exercises

Exercise	2D/3D	Number of sub-problems	Description
TD0	2D	5	Step insertion of 10% of rod length, followed by step removal of 5%, another 5% later.
TD1	2D	5	Linear insertion of 1% of rod length, followed by linear removal of a full 1% of the rod.
TD2	2D	3	Linear insertion of 10% of rod length, followed by linear removal of a full 10% of the rod.
TD3	2D	4	Linear decrease of water density, followed by a linear increase to original density.
TD4	3D	5	Linear insertion of 33.33% of rod length, followed by linear removal of full 33.33% of the rod.
TD5	3D	4	A linear decrease in water density, varying by location, followed by returning to original density.

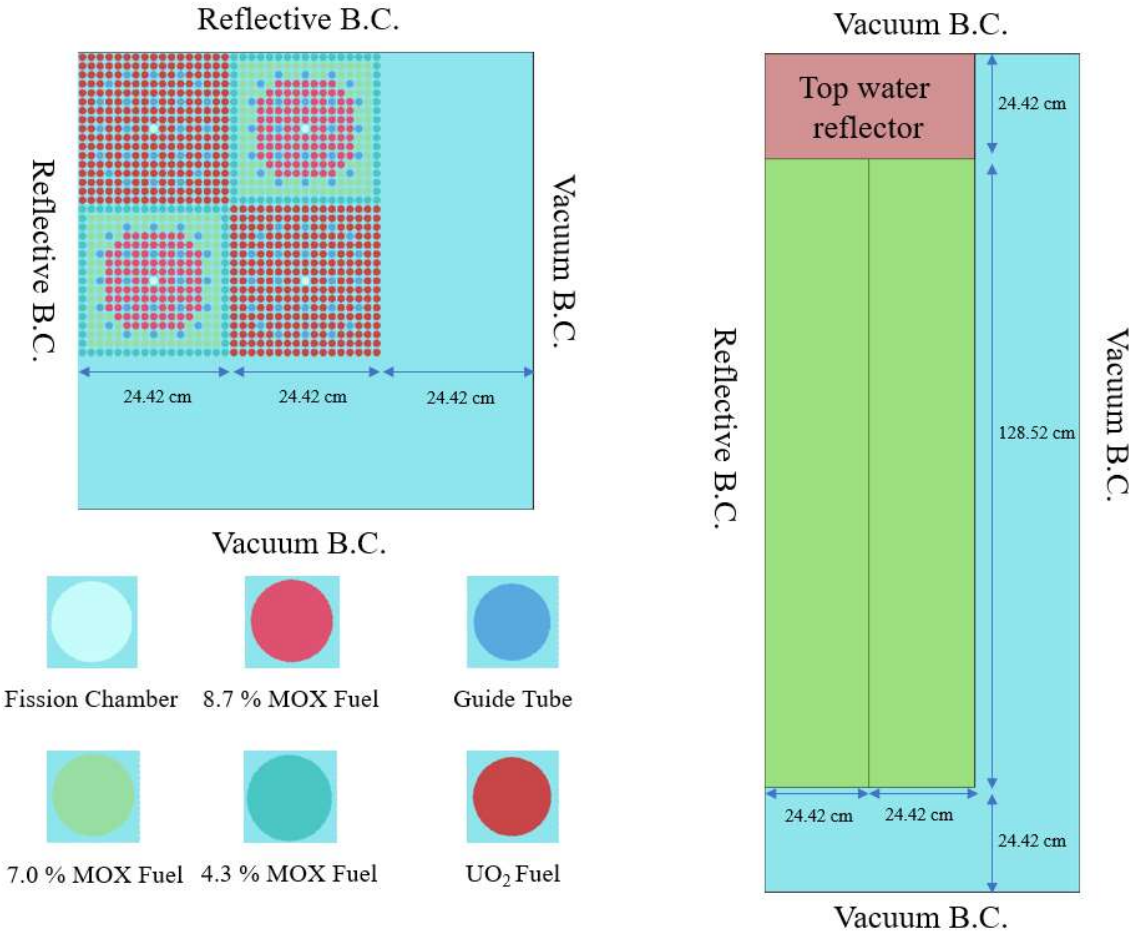

Figure 7 Planar and axial section configuration for the C5G7 benchmark problem

4.2 Simulation result of 2-D problems in C5G7-TD transient benchmark

The 2-D problems contain four distinct problems can be categorized into 2 types: Control rod insertion/withdrawal and the moderator density variation. Each of them contains their sub-problems. The control rod motion in problems TD0 through 2 is modeled by a time-dependent change in the absorption XS, which is either step or ramp change. The TD3 involves the ramp changes in moderator density. The result in the k_{eff} at the steady-state show excellent agreement with the reference as shown in Table II. This result indicates the fidelity of the initial simulation.

Table II Steady-State 2D Model k_{eff}

Code	k_{eff}	Difference (pcm)
MCNP [10]	1.18646 $\pm$ 0.008 (%)	-
DeCART	1.18660	14
STREAM	1.18664	18

a) Exercise TD0

In the TD0 problems, the control rod insertion and withdrawal movement are simulated by the assumption as a step change in the material composition, particularly an abrupt variation in XS for the guide-tube cell to control rod cell in fuel region shown in Fig. 8. The TD0 set consists of five sub-problems shown below:

- TD0-1: insertion/withdrawal of bank 1;
- TD0-2: insertion/withdrawal of bank 3;
- TD0-3: insertion/withdrawal of bank 4;
- TD0-4: insertion/withdrawal of banks 1,3 and 4 simultaneously;
- TD0-5: insertion/withdrawal of all banks

The power level changes generated by STREAM for the TD0 set is given in Fig. 9. Due to the sudden change of cross-section of the control rod material, the fission rate varies dramatically result in the total power declines abruptly from 0 s to 1 s, then increases dramatically at 2 s. In such cases, the time step is required to be small enough to satisfy the accuracy criteria. In this problem, at the abrupt change in the cross-section of the material, the time step is 0.1 ms while other using 0.25 ms as suggested from the benchmark. As the concentration of the delayed neutron precursors decreases during the transient, the total power reaches a smaller level than the initial state. Theoretically, if the transient time goes to infinity, the power level would approach to the initial value. To illustrate the change in the precursor density, Fig. 10, and Fig. 11 display for the longest-lived precursor group and the shortest-lived precursor group for case TD0-1, respectively. The behavior of the power level agrees very well with the result from nTRACER [14] with the maximum, average and the root mean square (RMS) of the relative error between the two codes for each sub-problem is given in Table III.

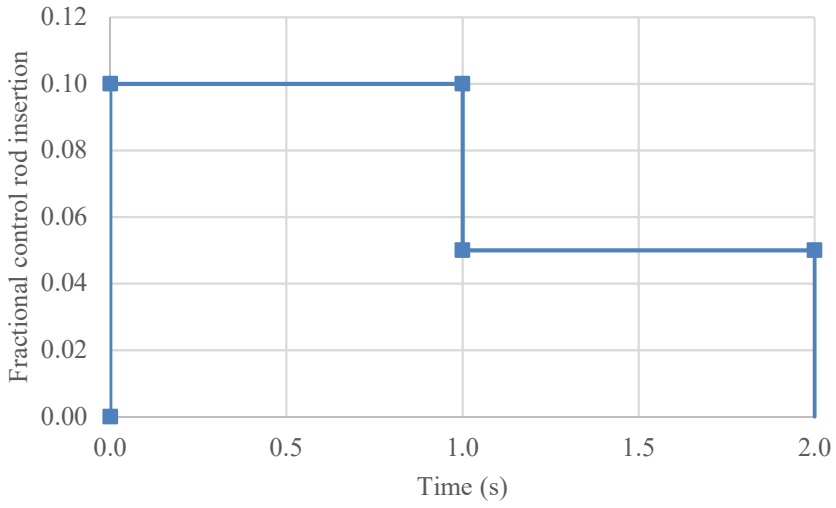

Figure 8 Control rod movement in TD0 transient exercise

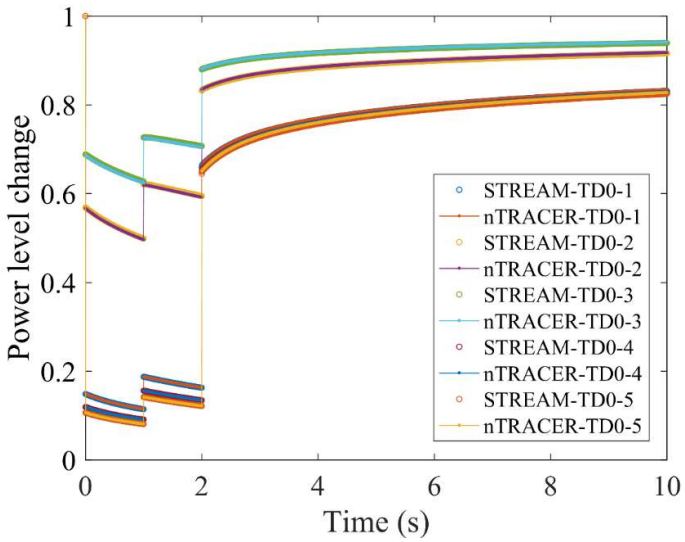

Figure 9 Power level change result from STREAM for TD0 transient exercise

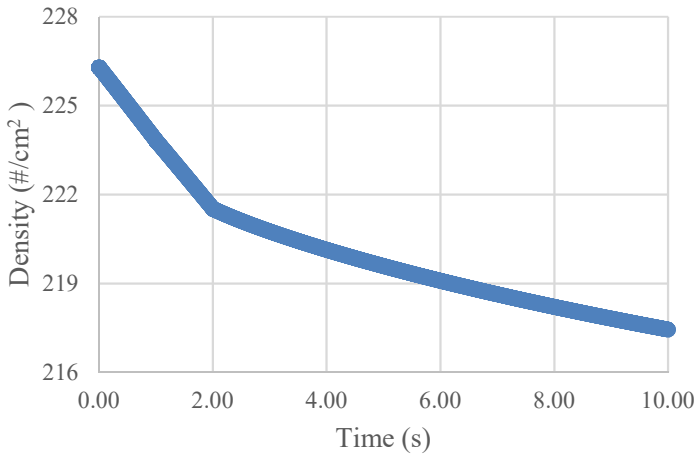

Figure 10 Density change of the longest-lived delayed neutron precursor group for case TD0-1

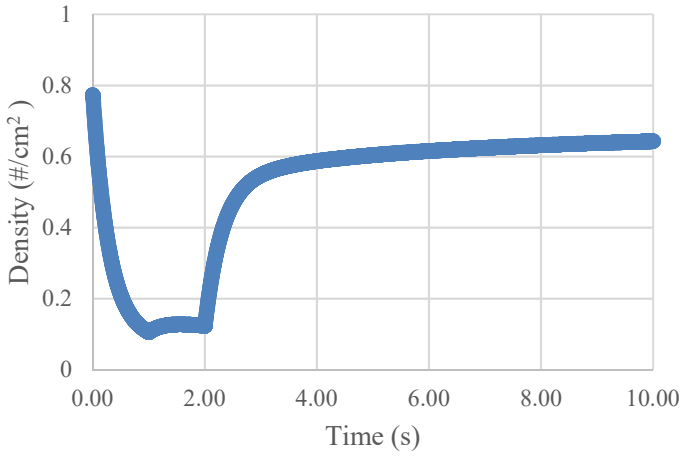

Figure 11 Density change of the shortest-lived delayed neutron precursor group for case TD0-1

For the longest-lived precursor, the declined slope mainly depends on the change of fission rate change due to the variation of the total absorption cross-section change. After the control rods are entirely removed, the density decreases based on the decaying process with the half-life approximately 1 minute. In the case of the short-lived precursor, the decaying process happens very fast (~0.2 s), after the control is inserted, the production rate of this group decreases vastly. After the withdrawal of the control rod, the production rate increase leads to the increase in the density curves, as shown in Fig. 11. Physically, these changes are the dominant effect explaining the declining sloped after the control inserted and remained position, i.e., between 0 and 1 sec, and 1 and 2 seconds.

Table III Comparison in the relative error (%) between STREAM and nTRACER for the TD0

Case ID	RMS	Max	Avg.
TD0-1	0.33	0.93	0.32
TD0-2	0.26	0.47	0.24
TD0-3	0.23	0.51	0.20
TD0-4	0.31	0.96	0.29
TD0-5	0.31	0.96	0.28

b) Exercise TD1 and TD2

The process of control rod insertion and withdrawal is simulated by the linear variation of the cross-section of the material in these two problems. The control rods are simulated with the movement at constant speed resulted in a ramp reactivity insertion. At the beginning of the simulation, all control rods are withdrawn, and at the end of 1 s, the fraction of control depth in the core reaches a specific value, where it is 1 % for TD1 and 10% for TD2 which is illustrated in Fig. 12. The control rod withdrawal procedure is conducted with the same speed and return to the initial state at the end of 2 s. Similarly, as in TD0, the TD1 and TD2 includes five sub-problems for each exercise shown below:

- TD1-1/TD2-1: insertion/withdrawal of bank 1;
- TD1-2/TD2-2: insertion/withdrawal of bank 3;
- TD1-3/TD2-3: insertion/withdrawal of bank 4;
- TD1-4/TD2-4: insertion/withdrawal of banks 1,3 and 4 simultaneously;
- TD1-5/TD2-5: insertion/withdrawal of all banks

The solutions in the power level change generated by STREAM given in Fig. 13 and Fig. 14. As expected, one can observe the continuous decrease in the total power during the cross-section changing period. A symmetric trend is observed in the total power change because of the symmetricity in the variation function of the cross-section. The deeper insertion of the control rods in the exercise

TD2 induced more negative reactivity compared to the TD1. As in the Fig. 13 and Fig. 14, excellent agreement with nTRACER results is observed. Table IV and Table V illustrate the maximum, average, and RMS of the relative error between the two codes for each sub-problem of TD1 and TD2 exercise, respectively.

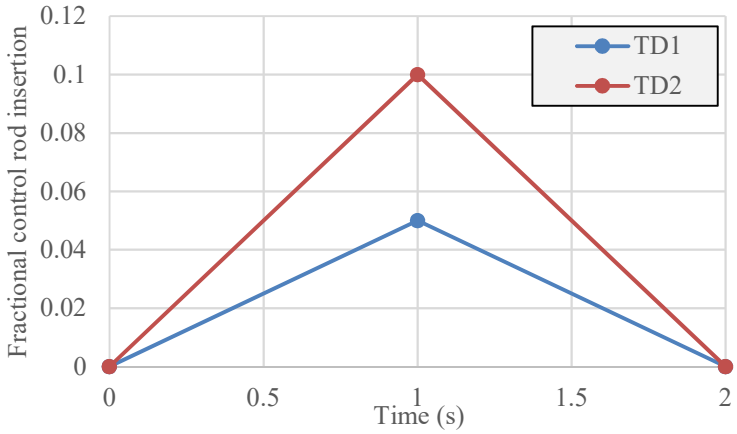

Figure 12 Control rod movement in TD1 and TD2 transient exercise.

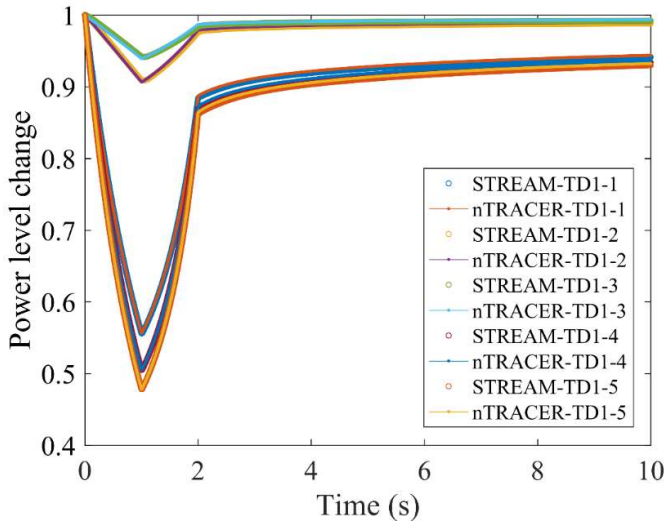

Figure 13 Power level change result from STREAM for TD1 transient exercise

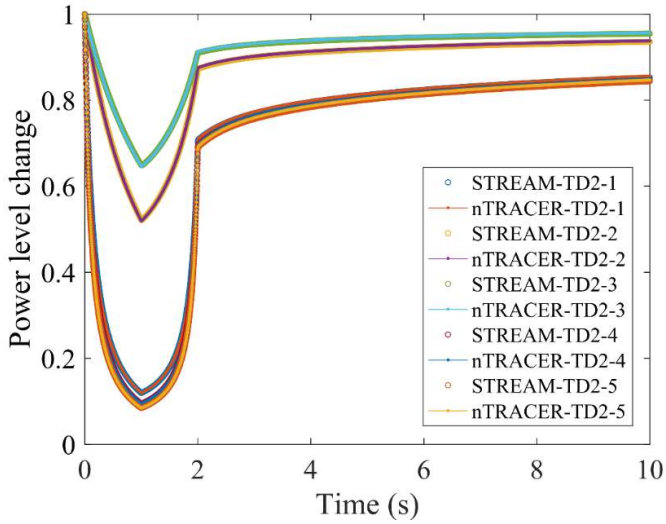

Figure 14 Power level change result from STREAM for TD2 transient exercise

Table IV Comparison in the relative error (%) between STREAM and nTRACER for the TD1

Case ID	RMS	Max	Avg.
TD1-1	0.26	0.38	0.25
TD1-2	0.17	0.35	0.17
TD1-3	0.16	0.34	0.15
TD1-4	0.26	0.38	0.25
TD1-5	0.26	0.37	0.25

Table V Comparison in the relative error (%) between STREAM and nTRACER for the TD2

Case ID	RMS	Max	Avg.
TD2-1	0.36	0.90	0.35
TD2-2	0.23	0.44	0.23
TD2-3	0.20	0.45	0.19
TD2-4	0.32	1.10	0.30
TD2-5	0.31	1.20	0.29

c) Exercise TD3

In the exercise TD3, the total moderator density in the cores is varied. It initially started with a normal condition density then reduces with a constant speed to the end of 1 s. After it reaches the minimum value, it returns to the initial with the same speed at the end of 2 s. This process is described in Fig. 15, which includes four sub-problems with their own variation factors. The result of this exercise is given in Fig. 16. Because of the linear change in the reactivity, the power level change shape shares

the similarity with exercise TD1 and TD2. Unquestionable, in the case of using changing factors 0.8, the power reaches the minimum value compared to the rest.

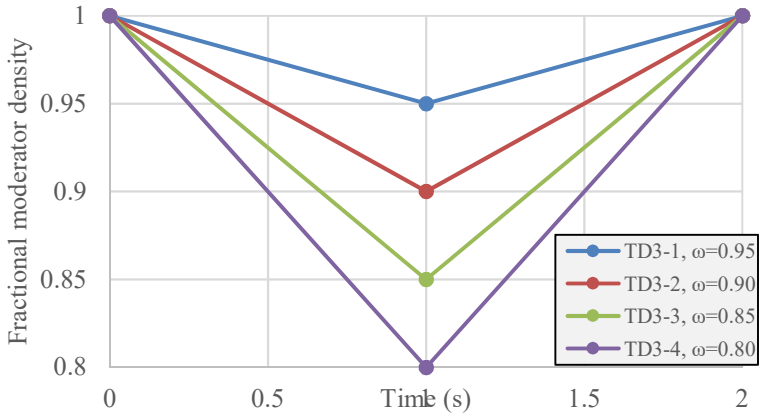

Figure 15 Core average moderator density change in TD3 exercise

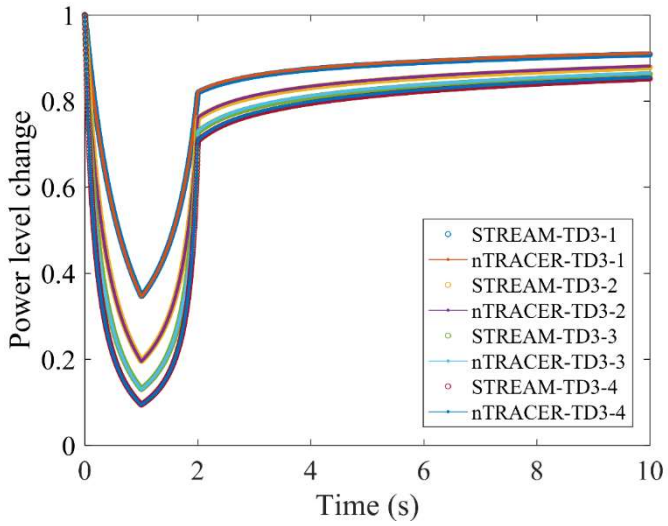

Figure 16 Power level change result from STREAM for TD3 transient exercise

As indicated in Table VI, good agreements between the two codes are observed. Moreover, as one may notice that the discrepancy in the case of the case TD3, the maximum value in relative error raise approximate 0.2 % for 5 % density reduced in the moderator. This error can be explained as the accumulated error from the difference between the nTRACER and STREAM code. As initially, with 95 % of moderator density, the maximum error is 0.64 %, while the fraction of change becomes 0.8, the maximum error reaches 1.22 % which means 0.6 % is accumulated to the error.

Table VI Comparison in the relative error (%) between STREAM and nTRACER for the TD3

Case ID	RMS	Max	Avg.
TD3-1	0.32	0.64	0.29

TD3-2	0.38	0.81	0.35
TD3-3	0.41	1.00	0.38
TD3-4	0.44	1.22	0.39

4.3 Decusping method and simulation result of 3D problems in C5G7-TD transient benchmark

In the analysis of 3D power reactors, the calculation with the control movement is a norm, and it requires the accurate modeling of the control rod inducing an immense perturbation on the reactivity lead to the change in power distribution. The substantial issue of this control rod modeling is usually involved with misalignment of the control rod tip and the axial mesh structure. It is necessary to resolve this problem appropriately because the movement of the control rod varies during the operation period and leads to the arbitrary axial position of the control rod tips. The below section presents the method to handle this issue.

a) Decusping Method for control rod movement

The most common and direct to solve this issue is to employ and introduce the adaptive mesh for regions where the control rod misaligned with the initial axial mesh. This approach is a straightforward one to handle the decusping; however, it requires intensive programming functions, including coding maintenance; thus, it is not so attractive to most of the reactor analysis tools. An alternative for this approach is the homogenization of the cross-section of inconsistent material in the axial mesh structures. The essential advantage of the homogenization is in the ease of implementation; however, it is necessary to determine a proper algorithm to calculate the homogenized cross-section. The strong neutron absorption of the control results in the harsh variation in the thermal flux in the neighbored regions with the control tips. Originally, the simple volume weighting scheme was introduced for homogenization, but it resulted in the over-prediction of the control rod effect, i.e., the cusping effect [15] illustrated in Fig. 17. Intricate researches on the homogenization schemes [16, 17] have been conducted and adopted to nodal analysis codes to mitigate the cusping effect. The principle of the decusping method is to use flux-volume weighting homogenization based on the generation of the axial flux for rodded and un-rodded regions by introducing a local 1D calculation. If the axial profile in the partially inserted control rod mesh with the height of h shown in Fig. 18 is obtained, the cross-section homogenization is introduced as in Eq. (4.1) below:

$$\Sigma_{r,g}^{h} = \frac{\Sigma_{r,g}^{R}\phi_{axial,g}^{R}h_R + \Sigma_{r,g}^{UR}\phi_{axial,g}^{UR}h_{UR}}{\phi_{axial,g}^{R}h_R + \phi_{axial,g}^{UR}h_{UR}} \ . \tag{4.1}$$

where the rodded and un-rodded are denoted by the super-script R and UR, respectively; r indicates the type of cross-section.

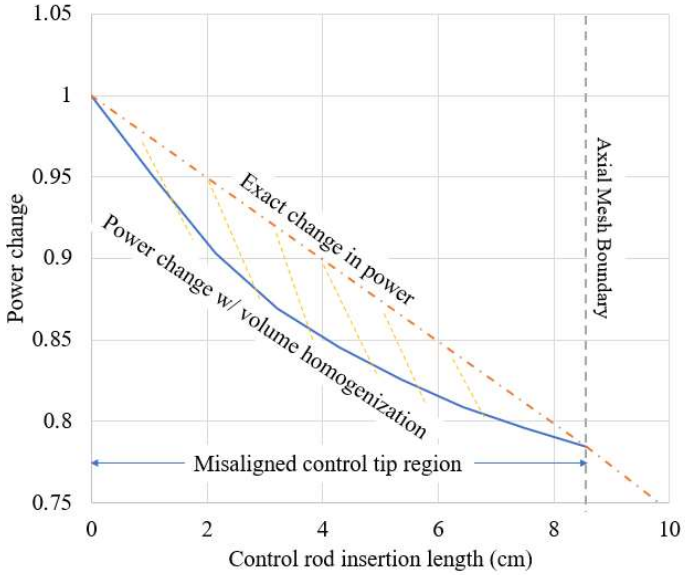

Figure 17 Control rod cusping effect on the total power by volume weighting

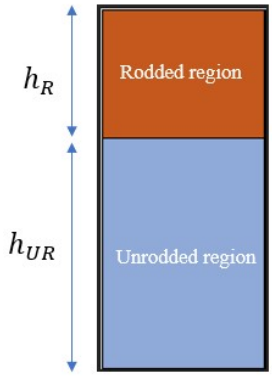

Figure 18 Illustration of partially inserted control rod axial mesh

The calculation of the axial flux profile can be achieved efficiently based on a local 1D solver because the control rod absorption appears and effects significantly to the thermal neutrons. While the mean free path of the thermal neutron in a typical PWRs is only few centimeters, thus the axial flux can be achieved in a local domain instead of the global whole core domain. In this research, the local domain contains 3 axial meshes of the interested fuel assembly where the misalignment of the control rod tips occurs with the boundary conditions are reflective for all directions. Initially, the boundary condition for the local 1D problem is taking the currents from neighboring fuel assemblies; however, the essential purpose of the local problem is to the axial flux in the control rod pin located several centimeters far from the interfaced surface. Thus the impact using the reflective boundary condition is insignificant. Furthermore, it also alleviates the complexity in implementation procedure. The local 1D solver is based on the nodal Finite Difference Method (FDM) with the local axial mesh height is equal to the control rod moving size over a time step. Because the local domain size is relatively small compared to the

global problem, this calculation is carried online with the transport calculation and thus cost an insignificant computational time contributed to the total time of the transient simulation. The group constant for the FDM solver is prepared from the global 3D transport calculation for fully rodded and un-rodded control rod configurations with the same mesh size as in the initial transport problem. Thus, similarly to the sub-plane scheme [18], in the fine mesh structure of the local FDM problem, it can be configured based on the achieved two sets of cross-section data. The cross-section data of the coarse plane is then assigned for its refined planes in the axial profile calculation with the corresponding control rod configuration.

During the implementation of the decusping method, for a control pin, the spatial self-shielding for the radial direction shown in Fig. 19 is not considered; thus, only one axial flux profile is applied for all radial regions of the pin. This misconception has a significant impact on the effectiveness of the current decusping method. Therefore, to resolve this issue, the pin-based flux distribution for rodded and un-rodded configurations is added to Eq. 4.1 during the homogenization process, as shown below:

$$\Sigma_{i,r,g}^{h} = \frac{\Sigma_{i,r,g}^{R}\phi_{axial,g}^{R}\phi_{radial,i,g}^{R}h_R + \Sigma_{i,r,g}^{UR}\phi_{axial,g}^{UR}\phi_{radial,i,g}^{UR}h_{UR}}{\phi_{axial,g}^{R}\phi_{radial,i,g}^{R}h_R + \phi_{axial,g}^{UR}\phi_{radial,i,g}^{UR}h_{UR}} \ . \tag{4.1}$$

with $\phi_{radial,i,g}^{R}$ and $\phi_{radial,i,g}^{UR}$ denotes for the radial flux distribution of the rodded and un-rodded regions for the radial region i respectively.

Notably, the flux used for the cross-section homogenization is a combination of both axial and radial flux profile. By applying this combination, the decusping method can resolve the spatial self-shielding issue in the homogenization. The radial flux distribution is obtained at the same time with the cross-section preparation for the local FDM 1D problem process. Thus the additional computational time for this process is negligible during the whore-core calculation.

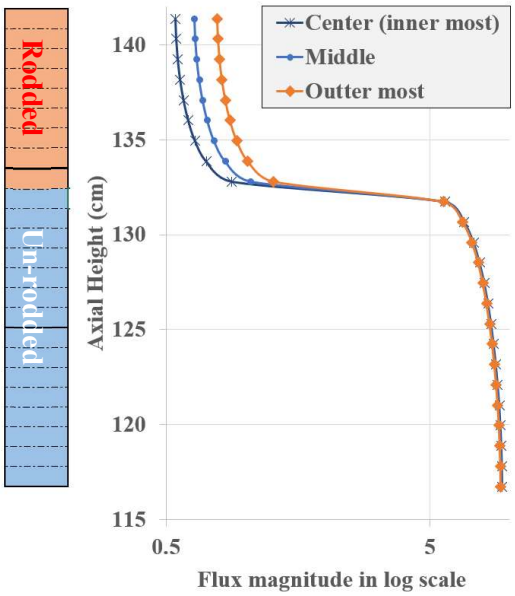

Figure 19 Illustration of the radial spatial self-shielding effect for the thermal flux of the partially rodded axial mesh

In order to have a more specific explanation for the decusping method, it will be illustrated comprehensively for the TD4-1 problem in the TD4 exercise in below section.

b) Exercise TD4

Exercise TD4 is a 3D time-dependent benchmark involving the process of control insertion and withdrawal. At the beginning of the simulation, the control rods are modeled in the top reflector region. The control rod is simulated to be fully inserted in the active core high within 6 s. Depending on the selection of control rod banks in different fuel assemblies, there are 5 sub-problems in this exercise shown in Fig. 20. The decusping method applied for this exercise is explained in detail for the case TD4-1. For this simulation, the model uses 0.05 s as the time step, the radial region for fuel pin and control rod pin are 5 and 3, respectively, as illustrated in Fig. 21. In order to keep the consistency with the reference result from nTRACER, the number of azimuthal angles is set as 64, and the polar angles in solid octant angle are 4.

Fig. 22 displayed the total power level change for the case TD4-1 with several axial mesh size using volume-weighting instead of using the decusping method. Obviously, as expected, the prompt drop appears at the very beginning due to the overestimation of the control rod effect. The curves should have the shape similar to the explicit model, i.e., using the axial mesh that equal to one control rod length inserted per one-time step, which costs tremendous computational time. For that reason, the decusping method undoubtedly must be applied. The local 1D FDM problem used for the decusping treatment is obtained with a single assembly with 3 axial nodes configuration. In the model where the decusping correction is applied, 15 axial meshes is used.

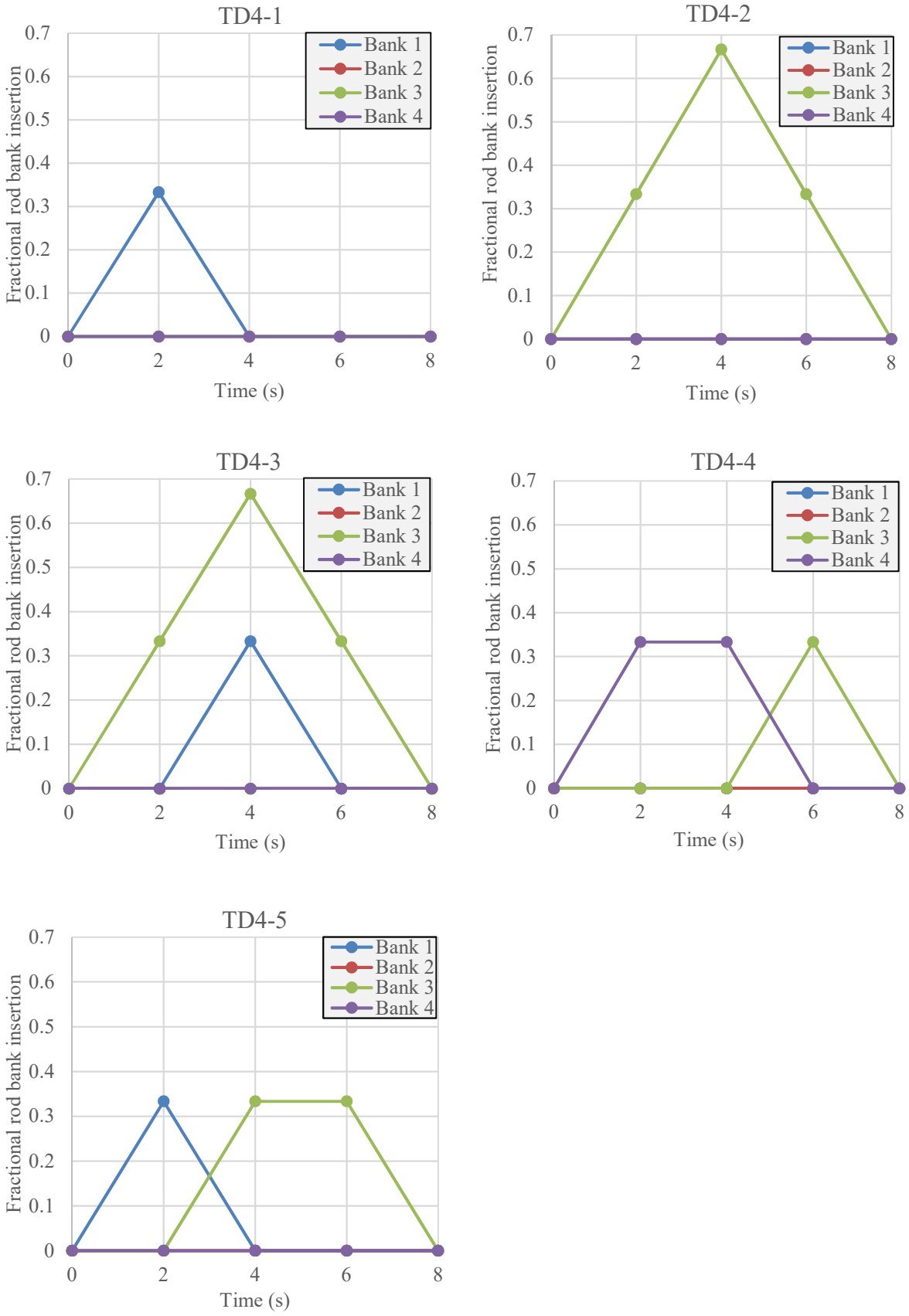

Figure 20 Relative inserted and withdrawn depth of control rod banks

For the sake of illustration of the local flux, the local flux profile for a single control rod pin partially inserted in one axial mesh shown in Fig. 23. As can be observed, the variation of the fast flux inside the interested axial mesh is smoother than that of the thermal flux. By using this axial flux profile combined with the radial flux for the control pin, the cusping effect is dramatically reduced, as shown in Fig. 24. The curve of the power level changes history simulated up to 8 sec. shows good agreement with the explicit model. Furthermore, the discrepancy with nTRACER reaches its maximum value at 2.74 % when the average value is 1.52 %. The main source of error is induced by the differences in the decusping methods and the 2D/3D DD method compared with the 2D/1D method.

Figure 21 Illustration of Fuel pin (Left) and Control rod pin (Right) with radial rings used in C5G7-TD benchmark

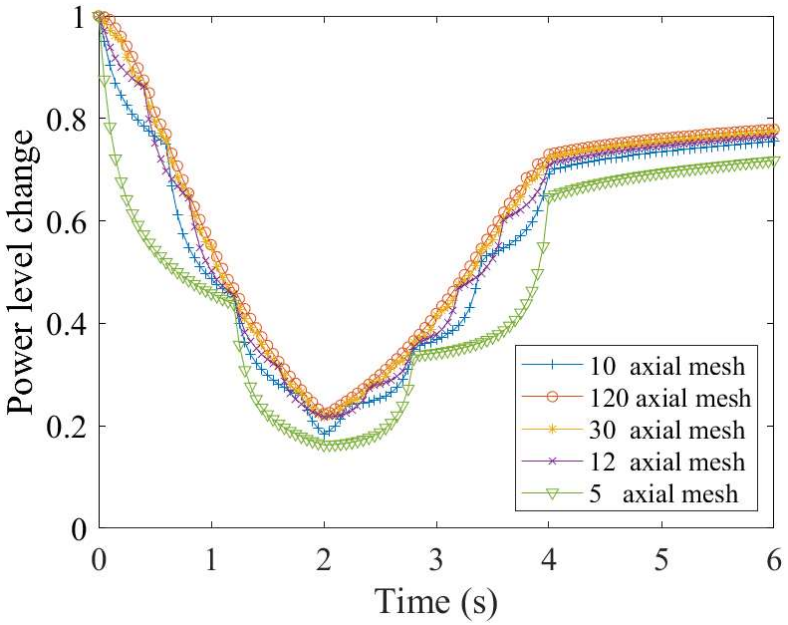

Figure 22 Power level change for TD4-1 case using various axial mesh size.

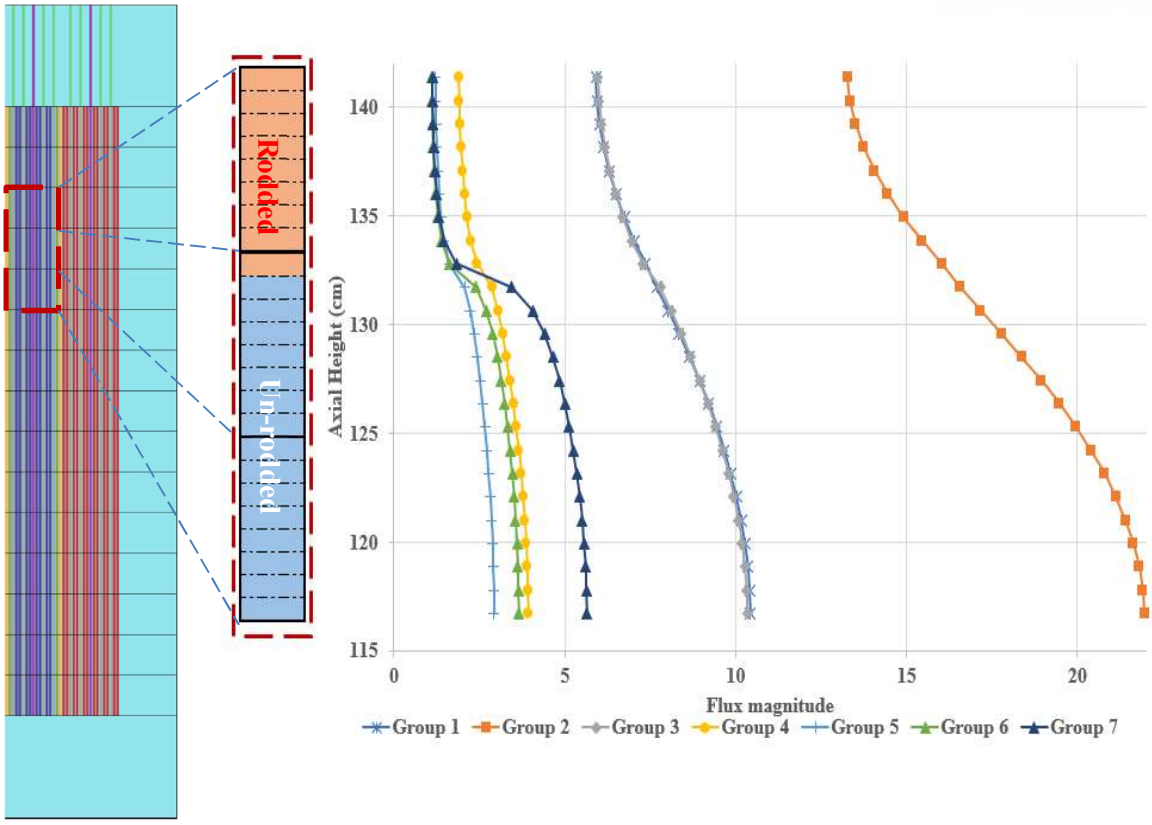

Figure 23 Illustration the axial section (Left) 1D local problem and the local flux shape for one control rod pin with reflective boundary condition (Right)

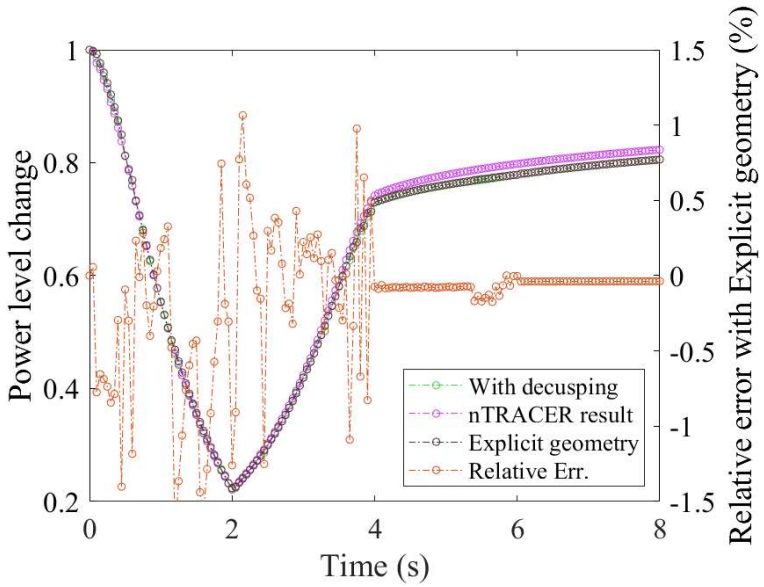

Figure 24 Power level change for TD4-1 case with control rod decusping correction.

By applied the same simulation condition and the decusping method model, the results in the power level for remaining sub-problems for this exercise is given in Fig. 24. The maximum amplitude of the relative error is about 3.2% between the STREAM and nTRACER, as shown in Table. VII.

Table VII Comparison in the relative error (%) between STREAM and nTRACER for the TD4

Case ID	RMS	Max	Avg.
TD4-1	1.75	2.74	1.52
TD4-2	1.52	2.98	1.48
TD4-3	1.30	2.80	1.32
TD4-4	1.73	3.20	1.40
TD4-5	0.89	2.43	1.03

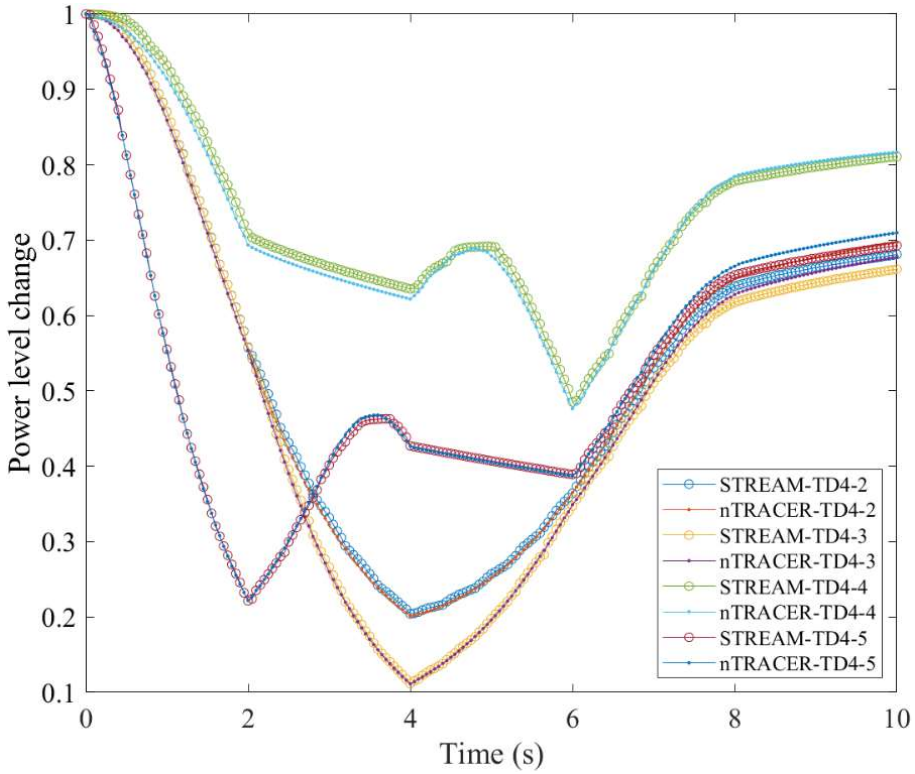

Figure 25 Power level change result from STREAM for TD4 exercise.

As observed in Fig. 24, the cusping effect has been mitigated properly by using the proposed decusping method for cases TD4-2,5. The STREAM result shares the similarity with the nTRACER's result for the power changing curves. However, as mentioned above, the main source of discrepancy is originated from the differences in the whole core transport method and the decusping method between the two deterministic codes. This difference results in the fission source magnitude gradually diverged from each other.

c) Exercise TD5

Instead of the insertion and withdrawal of the control rods, exercise TD5 is based on the density variation of the moderators. All control rods in this exercise are located in the fully un-rodded configuration. There are 4 sub-problems differentiated by the magnitude of density change in moderator

in different fuel assemblies shown in Fig. 26 [13]. The power level changes for TD5 exercise are depicted in Fig. 27. The agreement is improved in this exercise than in TD4 results; however, the discrepancy is still observed after the variation is stopped. The maximum, average, and the RMS of the relative errors are given in Table. VIII.

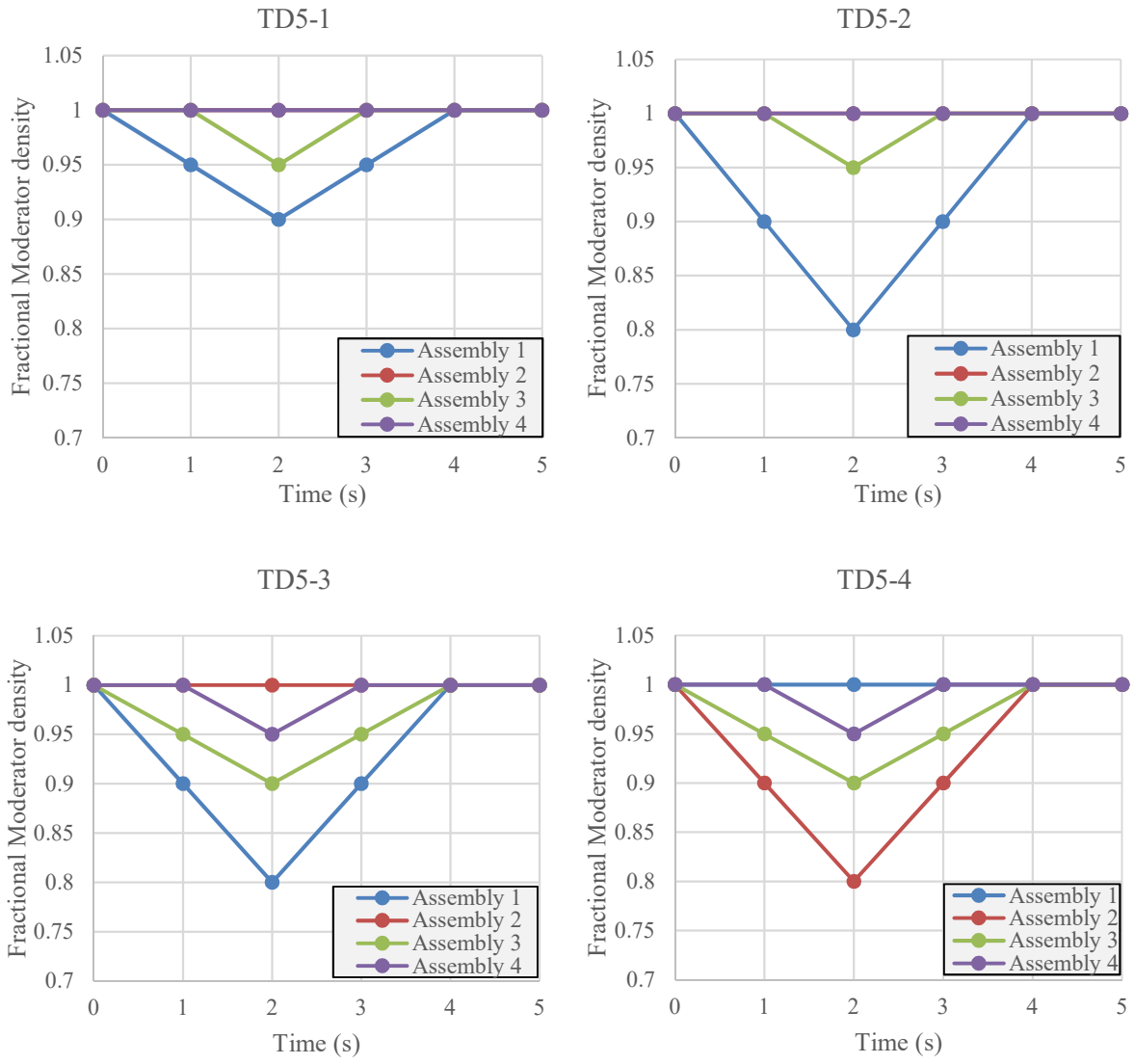

Figure 26 Relative moderator density in TD5 exercise

As expected, the effect on the moderator changes for assembly number 1st is dominant over the other assemblies. The least effective to the total fission rate is from assembly number 4th as it has a very small impact on power level change. For the sake of illustration of the impact on the power, the power distribution of TD5-4 case at 2 sec is given in Fig. 28. The symmetric trend is displayed similarly to the exercise TD3 due to the symmetric change of the moderator density.

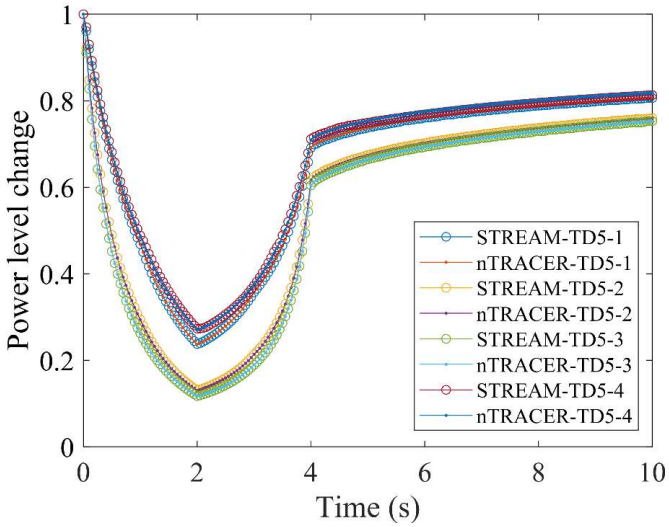

Figure 27 Power level change result from STREAM for TD5 exercise.

Table VIII Comparison in the relative error (%) between STREAM and nTRACER for the TD5

Case ID	RMS	Max	Avg.
TD5-1	0.59	0.75	0.58
TD5-2	0.41	0.67	0.40
TD5-3	0.63	0.79	0.63
TD5-4	0.85	1.37	0.84

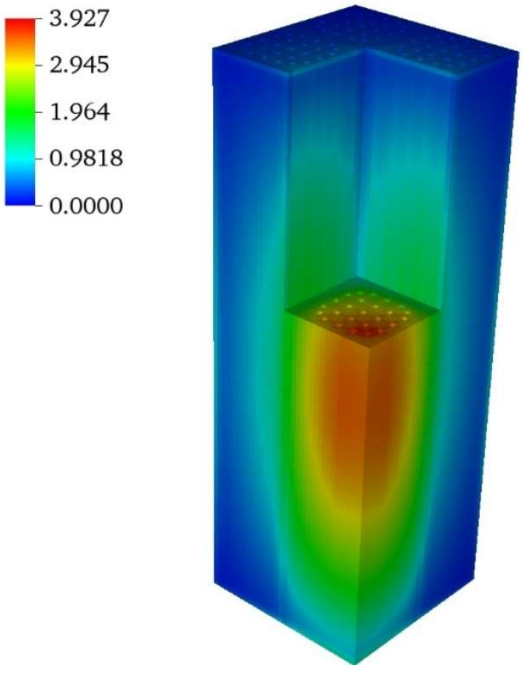

Figure 28 Power distribution at 2 sec for case TD5-4

V. Summary, Conclusion and Future work

In this research, the transport transient solver has been adopted to STREAM code and was examined by solving the neutron time-dependent benchmark C5G7-TD. The summary of the computational time and memory required for these calculations is displayed in Table. IX. The preliminary verification with reference solution from nTRACER show good agreement. For the 2D results, the maximum relative errors between the two codes for the total power level change is 1.22 % for the case of TD3-4 with the corresponding RMS is 0.44 %. For the 3D problems, due to the misalignment of the control rod tip issue when performing the control insertion and withdrawal transient simulation, a decusping method has been proposed. The overestimation of the control rods is mitigated effectively by applying the proposed method. The fundamental idea of the decusping method is to predict the axial flux in partially inserted control rod axial mesh and radial self-shielding treatment to capture the radial effect within the control rod pins to use as weighting function during the cross-section homogenization. By using the decusping method for 3D cases, the range of discrepancy in the relative errors between STREAM and nTRACER is 3.5 %. This difference is originated and accumulated due to the difference in the whole-core transport method and the decusping method between two codes. In the nTRACER code, larger axial meshes are used, and they consider the transport leakage in the 2D/1D approach while in STREAM, the axial mesh is much finer (~ 3cm), and no transport leakage is considered. However, whether or not additional factors can contribute to the calculation remains to be studied. In general, the results show very good agreement with the reference solution.

As shown in Table IX, the remaining issue for transient calculation in 3D geometry is that it required much more memory and longer computational time. Thus, the future work will concentrate on the improvement of the transient calculation performance by introducing different parallel algorithm and iteration scheme based on the CMFD instead of the MOC based scheme. Later on, the transient solver can be expanded to apply to realistic transient calculation and analysis coupled with TH1D feedbacks and multi-physic calculations.

Table IX Summary of the computational time and memory required to simulate the transient calculation up to 10 s

Case	Total memory (GB)	# CPUs	Time (h)	Case	Total memory (GB)	# CPUs	Time (h)
TD0-1	0.5	9	1.97	TD2-5	0.5	9	1.63
TD0-2	0.5	9	1.65	TD3-1	0.5	9	1.48
TD0-3	0.5	9	1.68	TD3-2	0.5	9	1.60
TD0-4	0.5	9	1.85	TD3-3	0.5	9	1.60
TD0-5	0.5	9	1.87	TD3-4	0.5	9	1.59
TD1-1	0.5	9	1.43	TD4-1	40.4	28	25.15
TD1-2	0.5	9	1.31	TD4-2	40.4	28	24.45
TD1-3	0.5	9	1.31	TD4-3	40.4	28	26.00
TD1-4	0.5	9	1.41	TD4-4	40.4	28	23.40
TD1-5	0.5	9	1.44	TD4-5	40.4	28	22.40
TD2-1	0.5	9	1.60	TD5-1	40.4	28	18.15
TD2-2	0.5	9	1.47	TD5-2	40.4	28	22.04
TD2-3	0.5	9	1.42	TD5-3	40.4	28	17.60
TD2-4	0.5	9	1.63	TD5-4	40.4	28	20.17

VI. References

[1] Sooyoung Choi, Changho Lee, Deokjung Lee, "Resonance Treatment using Pin-Based Pointwise Energy Slowing-Down Method," ***J. Comput. Phys***, http://dx.doi.org/10.1016/j.jcp.2016.11.007 (2017)

[2] Khang Nguyen Hoang Nhat, Sooyoung Choi, Matthieu Lemaire, Deokjung Lee*, "Depletion Chain Optimization of Lattice Code STREAM for PWR Fuel Assembly Analysis," ***Ann. Nucl. Energy***.

[3] Jiwon Choe, Sooyoung Choi, Peng Zhang, Jinsu Park, Wonkyeong Kim, Ho Cheol Shin, Hwan Soo Lee, Ji-Eun Jung, Deokjung Lee, "Verification and validation of STREAM/RAST-K for PWR analysis," ***Nuclear Engineering and Technology***, ISSN 1738-5733, https://doi.org/10.1016/j.net.2018.10.004 (2018)

[4] Y. Zheng, S. Choi, D. Lee, "A new approach to three-dimensional neutron transport solution based on the method of characteristics and linear axial approximation", ***Journal of Computational Physics***. vol **350**, pp. 25–44, 2017.

[5] Tomas Lefvert, "New applications of the collision probability method in neutron transport theory", ***Progress in Nuclear Engineer***, 1979, Vol ***4***, page 97-118.

[6] Lulu Li, Kord Smith, and Benoit Forget, "Techniques For Stabilizing Coarse-Mesh Finite Difference (CMFD) In Methods Of Characteristics (MOC)", *ANS MC2015 - Joint International Conference on Mathematics and Computation (M&C), Supercomputing in Nuclear Applications (SNA) and the Monte Carlo (MC) Method* · Nashville, Tennessee · April 19–23, 2015, on CD-ROM, American Nuclear Society, LaGrange Park, IL (2015)

[7] Boyd, William and Shaner, Samuel and Li, Lulu and Forget, Benoit and Smith, Kord, "The OpenMOC Method of Characteristics Neutral Particle Transport Code", ***Annals of Nuclear Energy***, Vol. **68**, page 43-52 (2014).

[8] H. G. JOO et al., "Methods and Performance of a Three-dimensional Whole-core Transport Code DeCART," ***Proc. PHYSOR2004***, Chicago, USA (2004).

[9] Cho, J. Y., K. S. Kim, et al. (2005). "Transient capability for a MOC-based whole core transport code DeCART." ***Transactions of the American Nuclear Society***, 92(Copyright 2006, IEE): 721-722.

[10] M. HURSIN et al., "DeCART v2.05 Theory Manual," (2008).

[11] S. Shaner, B. Forget, and K. Smith, "Sensitivity Analysis and Performance of the Adiabatic, Theta, and Multigrid Amplitude Function Kinetics Methods in 2D MOC Neutron Transport," ***In: Proc. M&C 2013***, Sun Valley, ID, May 5-9, (2013)

[12] A. Zhu, et al., "Transient Methods For Pin-Resolved Whole Core Transport Using The 2D-1D Methodology In MPACT", ***Proc. M&C 2015***, American Nuclear Society, Nashville, TN, USA, April 19-23, (2015)

[13] Victor F. Boyarinov, Peter A. Fomichenko, et al., "Deterministic Time-Dependent Neutron Transport Benchmark without Spatial Homogenization (C5G7-TD)", Vol. 1, **NEA/NSC/DOC** (2016)

[14] Min Ryu and Han Gyu Joo, "nTRACER Whole Core Transport Solution to C5G7-TD Benchmark", **M&C 2017** - International Conference on Mathematics & Computational Methods Applied to Nuclear Science & Engineering, Jeju, Korea, April 16-20, 2017, on USB (2017)

[15] Y. S. JUNG and H. G. JOO, "Control Rod Decusping Treatment Based on Local 3-D CMFD Calculation for Direct Whole Core Transport Solvers," in "***Proceedings of the International Congress on Advances in Nuclear Power Plants (ICAPP)***," (April 6–9 2014).

[16] Aaron M. Graham, Benjamin S. Collins and Thomas Downar, "Subplane-based Control Rod Decusping Techniques for the 2D/1D Method in MPACT", **M&C 2017** - International Conference on Mathematics & Computational Methods Applied to Nuclear Science & Engineering, Jeju, Korea, April 16-20, 2017, on USB (2017)

[17] T. Downar, Y. Xu V. Seker, "PARCS Theory manual."

[18] C. Y. Cho, H. G. Joo et al., "Axial SPN and Radial MOC Coupled Whole Core Transport Calculation," **J. Nucl. Sci. Technol**., 44, pp. 1156-1171 (2007).

Acknowledgement

This master thesis would not have been possible without the support of several people. First of all, I would like to express my sincere gratitude to my advisor and committee chair Prof. Deokjung Lee, who has guided my academic development and provided a constant example of integrity and dedication to research. I would also like to thank my committee members for their valuable feedback and guidance. I am also very grateful to Dr. Sooyoung Choi, who is a great mentor with profound patience to answer and explain my questions, no matter how naive or tricky they are.

I would also like to thank nTRACER team in Seoul Nation University for sharing their result to make it available for the verification in this thesis.

I feel I am incredibly indebted to my fellow seniors and lab mates: Dr. Peng Zhang, Dr. Jiankay Yu, Dr. Taewoo Tak, Dr. Matthieu Lemaire, Dr. Alexey Cherezov, Dr. Xianan Du, Dr. Hyunsuk Lee, Wonkyeong Kim, Jiwon Choe, Chidong Kong, Jinsu Park, Hanjoo Kim, Yunki Jo, Bamidele Ebiwonjumi, Kiho Kim, Sanggeol Jeong, Eun Jeong, Jaerim Jang, Nguyen Tung Dong Cao, Woonghee Lee, Tuan Tran Quoc, Yongmin Jo, Lezani Van Der Merwe, Mai Nhan Nguyen Trong, Vutheam Dos, Azamat Khassenov and all others for working together, supporting my studies in Korea.

Finally, I would like to thank to my family for their love and effort to raise me. I should also apologize to them for not being able to keep company with them when studying abroad thousands of miles away.